REVIEW

Check for updates

Halide solid-state electrolytes for all-solid-state batteries: structural design, synthesis, environmental stability, interface optimization and challenges

Boran Tao,[ab] Dailin Zhong,[a] Hongda Li, [ID] [ab] Guofu Wang[a] and Haixin Chang [ID] *[b]

Since the huge breakthrough in 2018, research on halide solid-state electrolytes (SSEs) has set off a new craze. In comparison with oxide and sulfide SSEs, halide SSEs have more balanced properties in various aspects, including ionic conductivity, electrochemical stability window, and moisture resistance. Herein, the overall knowledge and deep understanding of halide SSEs and their practical applications in all-solid-state batteries (ASSBs) are introduced. Firstly, the principle of screening halide SSE components is proposed. Among F, Cl, Br and I anions, the Cl anion is excellent owing to its suitable ionic conductivity and electrochemical stability window. The Sc, Y, and lanthanide elements are also more compatible with Cl anions in terms of electronegativity. Secondly, the structural design theory of halide SSEs with high ionic conductivity and the mechanism of Li ion migration are described. A monoclinic structure is more conducive to Li ion migration, compared with trigonal and orthorhombic structures. Additionally, substitution strategies for halide SSEs are discussed, mainly including dual-halogen, isovalent cation substitution, and aliovalent cation substitution. Furthermore, the mechanism of moisture resistance and synthesis method of halide SSEs are analyzed. Compared with the solid-state reaction and mechanochemistry method, wet chemical synthesis is more likely to achieve scale-up production of halide SSEs. Finally, the application prospects and challenges of halide SSEs in ASSBs are outlined.

[a]Liuzhou Key Laboratory of New-Energy Vehicle Lithium Battery, School of Electronic Engineering, Guangxi University of Science and Technology, Liuzhou, 545006, China
[b]Quantum-Nano Matter and Device Lab, State Key Laboratory of Material Processing and Die & Mould Technology, School of Materials Science and Engineering,

Huazhong University of Science and Technology, Wuhan, 430074, China. E-mail: hxchang@hust.edu.cn

Boran Tao is an assistant professor at the Guangxi University of Science and Technology. He got his PhD in Materials Science and Engineering in 2019 from Chongqing University. He is a visiting scholar at the Huazhong University of Science and Technology for research on new energy materials. His research focuses on solid-state electrolytes, anode materials, and cathode materials for Li ion batteries.

Haixin Chang is a full professor at the Huazhong University of Science and Technology. He got his PhD in Materials Science in 2007 from the Institute of Metal Research, Chinese Academy of Sciences. Then, he worked at the Department of Chemistry, Tsinghua University, and Nanotechnology Center, ITC, Hong Kong Polytechnic University, before moving to Tohoku University at the beginning of 2011. He joined the faculty of Tohoku University as an assistant professor in 2012. He joined the Huazhong University of Science and Technology as a full professor in 2014. His researches focus on 2D/quantum materials, 2D electronics/optoelectronics, and new energy materials. He has published over 100 papers with a citation over 6000 times. He was also awarded 2020–2022 Elsevier Highly Cited Chinese Researchers.

1. Introduction

Since the advent of lithium-ion batteries (LIBs), they have been widely considered a research hotspot.[1-4] The rapid development of electronics and electric vehicles has put forward higher requirements for rechargeable LIBs, including better safety, higher capacity, higher energy density, and faster charging performance. Faced with these growing demands, conventional LIBs with liquid electrolytes have not performed as expected. Hence, building next-generation "beyond Li-ion" batteries has been key to meet the increasing demands of the energy storage market.[5-7] One promising strategy is to assemble all-solid-state batteries (ASSBs) using solid-state electrolytes (SSEs) rather than liquid electrolytes found in conventional LIBs.[7-9]

According to the chemical composition, SSEs are broadly divided into three categories: inorganic electrolytes, polymer electrolytes and organic–inorganic hybrid composites.[10-12] Inorganic electrolytes have ionic conductivity comparable to that of liquid electrolytes, exhibiting a greater electrochemical stability window and wider operating temperature window, which provide new opportunities for the development of next-generation "beyond Li-ion" batteries.[7,13,14] Based on anion chemistry, inorganic electrolytes can be further divided into oxides, sulfides, and halides.[15,16] In contrast, halide SSEs are believed to be the best candidates for ASSB technology due to their intrinsic chemical properties (Fig. 1).[17-21] Firstly, the weaker Coulomb force between halogen anions and Li ions and the wider Li ion transport channel formed by relatively larger radius halogen anions ($Cl^- = 167$ pm, $Br^- = 182$ pm, $I^- = 202$ pm, $O^{2-} = 126$ pm and $S^{2-} = 170$ pm)[22,23] are conducive to ion mobility and guarantee the high ionic conductivity of halide SSEs (*e.g.*, Li_3ScCl_6,[24] 3.02 mS cm^{-1}). Secondly, halide SSEs still possess good air stability and recoverability after humidity exposure. Li_3InCl_6 remains stable after exposure to dry or low humidity air at ambient temperature.[25,26] This property can eliminate the need for a rigorous assembly environment for ASSB manufacturing, which is beneficial to significantly reduce production costs. Thirdly, halide anions have a higher electrochemical oxidation stability (such as up to ~4.21 V for Li_3YCl_6)[27] and can be more compatible with high voltage cathode materials, thus exhibiting good capacities. Finally, halide anions have lower bond strength with polyanions, softer lattice structures, and higher anionic polarizability than oxides and sulfides, which endows halide SSEs with better mechanical deformability and is beneficial for the assembly of ASSBs.[27-29]

In the 1930s, halide electrolytes were first studied and exhibited room-temperature ionic conductivity as low as 10^{-7} S cm^{-1}, so they didn't attract wide publicity.[30-32] Until 2018,
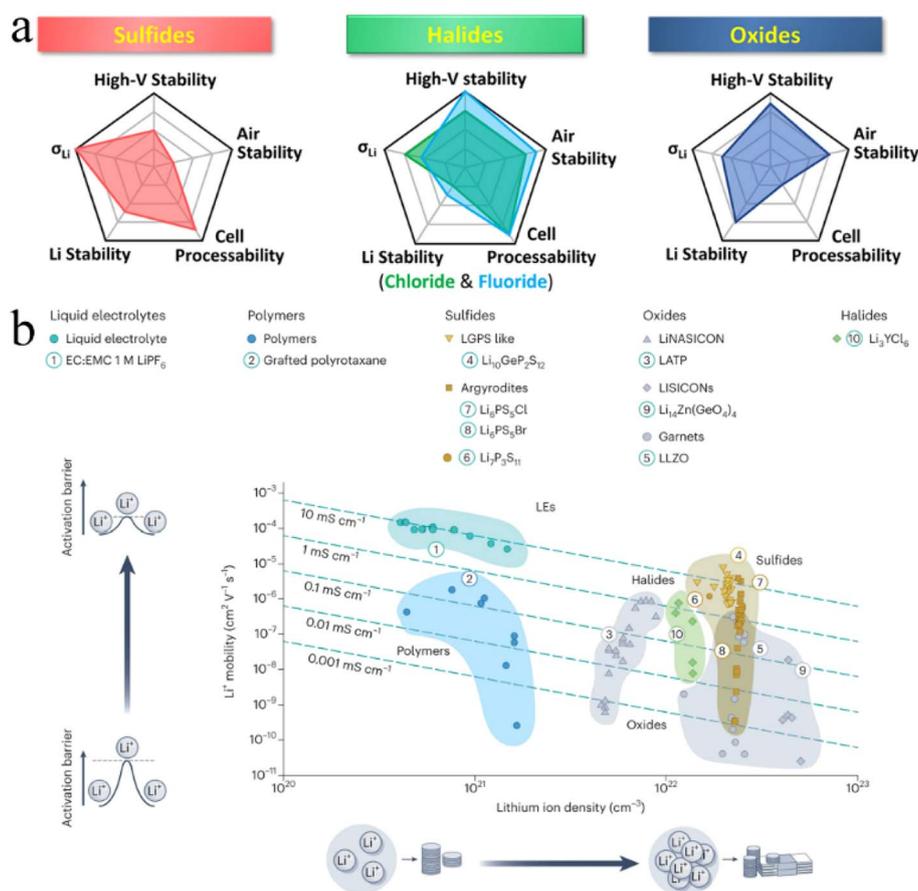

Fig. 1 (a) Spider plots exhibiting various properties of three typical inorganic SSEs. Reproduced with permission.[19] Copyright 2022, American Chemical Society. (b) Comparison of the ionic conductivity of different electrolytes based on the Li content. Reproduced with permission.[18] Copyright 2023, Springer Nature.

Asano *et al.* significantly increased the room-temperature ionic conductivity of halide SSEs to 1.7 mS cm^{-1}, which triggered a research hotspot in halide SSEs.[19,23,33–37] In terms of composition, fast Li-ion conductors based on ternary halides can be roughly divided into three categories: (i) Li_3MX_6 halide electrolytes with group 3 elements (M = Sc, Y, and lanthanides); (ii) Li_3MX_6 halide electrolytes with group 13 elements (M = Al, Ga, In); and (iii) Li_2MX_4 or Li_6MX_8 halide electrolytes with divalent metal elements (M = Ti, Zr, Hf, V, Cr, Mn, Fe, Zn, Mg).[34] In addition, there are quaternary halide compounds formed by chemical substitutions to improve ionic conductivity and humidity tolerance, *e.g.*, $Li_3Y_{1-x}In_xCl_6$,[38] $Li_{3-x}Er_{1-x}Zr_xCl_6$.[39] From another viewpoint, halide fast Li-ion conductors can be generally divided into four categories according to crystalline structures, including (i) trigonal structures (space groups: $P\bar{3}m1$), such as Li_3YCl_6,[33] and Li_3ErCl_6;[40,41] (ii) monoclinic structures (space groups: $C2/m$), such as Li_3YBr_6,[33] Li_3InCl_6,[42] and Li_3ScCl_6;[24] (iii) orthorhombic structures (space groups: $Pnma$), such as Li_3YbCl_6[43] and $Li_{2.5}Y_{0.5}Zr_{0.5}Cl_6$;[44] (iv) spinel structures (space groups: $Fd\bar{3}m$), such as $Li_2Sc_{2/3}Cl_4$,[45] $Li_2Sc_{3-x}Er_xCl_4$,[46] and Li_2FeCl_4.[47] In parallel, halide fast Na-ion conductors, mainly including Na_2ZrCl_6,[48] $NaAlCl_4$,[49] Na_3MCl_6 (M = Y, Er, In, Sc, and Yb),[50–52] Na_3MBr_6,[51,53] Na_3MI_6 (M = Sc, Y, La, and In),[54,55] $Na_{3-x}Y_{1-x}Zr_xCl_6$,[56,57] $Na_{3-x}Er_{1-x}Zr_xCl_6$,[58] $Na_2In_xSc_{0.666-x}Cl_4$,[59] and $Na_3In_{1-x}Sc_xCl_6$ (ref. 59) have also been investigated. However, there is still a large gap between the limited ionic conductivity (<0.1 mS cm^{-1}) of halide fast Na-ion conductors and the demand for practical applications. Besides, halide SSEs have the obvious advantage of abundant synthesis pathways, such as mechanochemical synthesis,[41,60] co-melting synthesis,[45] and wet chemical synthesis,[61–63] which can avoid the high-temperature sintering process used in sulfide and oxide SSE synthesis and greatly reduce energy consumption and manufacturing cost.

In this review, the present development of halide SSEs and their practical applications in ASSBs are introduced. Firstly, the principle of screening halide SSE components is proposed. Secondly, the structural design theory of halide SSEs with high ionic conductivity and the mechanism of Li ion migration are described. Additionally, substitution strategies for halide SSEs are discussed, including dual-halogen, isovalent cation substitution, and aliovalent cation substitution. Furthermore, the mechanism of moisture resistance and the synthesis of halide electrolytes are presented. Next, the application prospects and challenges of halide SSEs in ASSBs are outlined. Finally, the summary and outlook of future development and challenges for halide SSEs are also presented along with the discussions for their commercial applications in ASSBs.

2. Composition, structure, and ion migration mechanism of halide SSEs

The composition and structure of materials determine their intrinsic chemical properties to some extent. In the past few years, the discovery of new materials has seriously relied on the researcher's experience and intuition and then been further validated by synthesis and characterization in a laboratory, which is considered an inefficient, resource-consuming, and expensive process. There are more than 200 000 entries in the Inorganic Crystal Structure Database (ICSD).[64] If traditional trial-and-error approaches are used to screen them one by one, it can't meet the urgent demand for the development of new materials and energy technologies. Luckily, with the rapid development of material informatics, numerous advanced technologies such as artificial intelligence,[65,66] machine learning,[67,68] high-throughput screening,[40,69] *ab initio* molecular dynamics (AIMD),[70,71] density functional theory (DFT),[72] and first-principles calculations,[73–75] are used to guide component screening, structural design, and ion diffusion prediction of crystalline inorganic SSEs.

2.1 Component screening of halide SSEs

In halide SSEs, the elemental composition of the phase field determines the range of chemical structure and bonding, thus affecting the related properties. The common method of designing SSEs is to select suitable primary elements to construct a non-rigid frame for fast Li ion conduction and compact solid–solid contact. The elements that are applicable to halide SSEs are shown in Fig. 2.

Halides have become a better choice for SSE materials than oxides and sulfides. Muy *et al.*[40] used lattice-dynamics descriptors to screen more than 14 000 compounds, where 18 components were identified as the most promising fast Li-ion conductors according to computed Li-phonon band centers and electrochemical stability windows, including 4 fluorides, 9 chlorides, and 2 bromides. Among them, Li_3ErCl_6 was successfully synthesized and showed an ionic conductivity of 0.05–0.3 mS cm^{-1}, which well proved the rationality of prediction results. Based on a data-driven approach, 6600 materials containing O, S, F, Cl, Br, I, N, P, Ge, or Si monatomic anions were screened, among which only chlorides and bromides could exhibit both fast ionic conduction and high oxidation potential.[77] Rational selection of a halogen anion can also further improve the comprehensive performance of SSEs. Based on the DFT method, chlorides in trigonal halides Li_3MX_6 (X = Cl, Br, and I) exhibited faster ionic conductivity, a wider electrochemical stability window and a higher elastic modulus, which were more suitable for high-voltage cathodes.[78] The first-principles calculations of $Li_2Sc_{2/3}X_4$ (X = Cl, Br, and I) showed that the Cl anion was the best choice for superior performance in ASSB applications, due to its excellent ionic conductivity, electrochemical stability, and interfacial compatibility.[79] This was mainly attributed to the formation of an ion pair between Cl and Sc, leading to high ionic conductivity (2.07 mS cm^{-1}) and a wide electrochemical stability window (0.91–4.25 V). Consistent with this, the AIMD study for Li_3YX_6 (X = F, Cl, Br, and I) series showed that Li_3YCl_6 possessed the lowest activation energy and the highest ionic conductivity.[71] The octahedron–octahedron (Oct–Oct) Li ion diffusion pathway and weak coulombic force between Li and Cl ions were the main factors that made it outstanding. Unfortunately, Li_3YCl_6 was most energetically favorable to form an antisite defect and transform
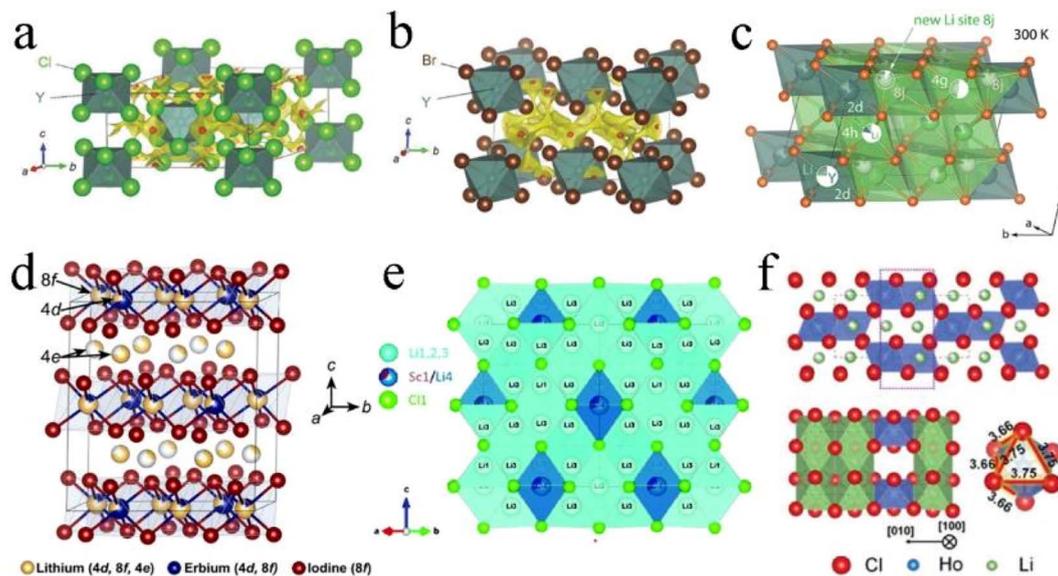
Fig. 2 Elements in the periodic table that are applied to halide SSEs. The unit of ionic radius is pm, and the data come from ref. 76.

into a lower ionic conductivity lattice, which made the experimentally measured ionic conductivity (0.51 mS cm^{-1}) of Li$_3$YCl$_6$ far away from the predicted value (10.4 mS cm^{-1}).[33,71]

Except for halogen anions, Li/cation configurations also have an important influence on ionic conductivity. The atomic size and valence electron configuration of non-mobile cationic elements determine their coordination environment and lattice volume and ultimately affect the corresponding ionic conductivity.[73] The 202 Li-containing chlorides in the ICSD were screened using first-principles calculations,[80] where 19 of them were considered potential Li superionic conductors ($\sigma_{Li} > 1$ mS cm^{-1} at room temperature), and their cations mainly included In, Mg, Zn, Zr, Er, Al, Sc, and Y elements. The low activation energy barrier for Li ion migration could be achieved in a target crystalline structure frame by adjusting the electronegativity difference between anionic and nonmobile cationic elements. Non-mobile cationic elements with high electronegativity were preferred for Li superionic conductors with a tetrahedral substructure. In contrast, non-mobile cationic elements with low electronegativity were preferred for Li superionic conductors with an octahedral substructure.[73,81] DFT calculations for Li$_3$MI$_6$ (M = Sc, Y, and La) showed that the key event to the extremely fast diffusion of Li ions in Li superionic conductors with an octahedral substructure lied in the large electronegativity difference between anion elements and non-mobile metal cation elemenst.[82] The high ionic conductivity of Li$_3$YBr$_6$, Li$_3$LaI$_6$, and Li$_3$ErI$_6$ was consistent with the octahedral principle.[33,82,83]

In general, Li$_3$MCl$_6$ (M = Sc, Y, and lanthanides) are the most potential halide SSEs, which can reconcile ionic conductivity with the electrochemical stability window.

2.2 Structural design of halide SSEs

The crystal structure of SSEs directly determines the diffusion pathway of Li ions and affects their ionic conductivity. The calculation result of sulfide indicated that body-centered cubic (bcc) allowed Li ions to hop directly from adjacent tetrahedral sites, with the lowest energy barrier and the highest ionic conductivity.[84] However, most halide SSEs had anion sublattices with a hexagonal close-packed (hcp) or face centered cubic (fcc) structure, which were beneficial for the higher electronegativity and lower polarizability of halogen anions compared with O^{2-} and S^{2-} anions.[27,80] For halide SSEs, the anion sublattice formed the framework of the crystal structure, where interstitial sites were occupied by Li ions and other cations. The anion sublattice was commonly hcp or cubic close-packed (ccp), while cation arrangement mainly depended on the component and synthetic method.[41,85–87] The crystallographic structure of halide SSEs was dependent on the ionic radius (r) of the central metal element. When r was less than or equal to 80 pm, halide SSEs tended to have a monoclinic structure. When r was between 80 pm and 85 pm, they exhibited a trigonal structure. When r was greater than or equal to 85 pm, they seemed to have an orthorhombic structure.[23,34,88] In general, ternary halides had five crystal structures, the monoclinic structure (space group $C2/m$, $C2/c$), halospinel structure (space group $Fd\bar{3}m$) with a ccp anion framework, orthorhombic structure (space group $Pnma$) and trigonal structure ($P\bar{3}m1$) with an hcp anion framework.

Li$_3$YCl$_6$ and Li$_3$YBr$_6$ were the earliest reported halide SSEs with high ionic conductivity.[33] Li$_3$YCl$_6$ had a trigonal structure and hcp anion framework with the octahedral coordination of all Cl atoms forming YCl$_6$$^{3-}$ and LiCl$_6$$^{5-}$ octahedra and the six LiCl$_6$$^{6-}$ octahedra surrounding every YCl$_6$$^{3-}$ octahedron (Fig. 3a).[27,33] Y atoms occupied two distinct sites. One was a 1a site where the YCl$_6$$^{3-}$ octahedra were isolated from each other and were completely occupied by Y. Another one was a 2d site where the YCl$_6$$^{3-}$ octahedron shared a face along the c-axis direction and exhibited a noteworthy Y disorder. Li occupied 6g and 6h sites in whole or in part, forming chains with face-sharing along the c-axis direction and edge-sharing within the

Fig. 3 The crystal structures of (a) Li_3YCl_6 and (b) Li_3YBr_6 refined by Rietveld analysis and superimposed with a Li ion potential map. Reproduced with permission.[33] Copyright 2018, Wiley–VCH. (c) The additional Li ion occupying interstitial 8j sites that connect 4g and 4h sites by face sharing in Li_3YBr_6. Reproduced with permission.[91] Copyright 2020. American Chemical Society. (d) The crystal structure of Li_3ErI_6, where the Li occupies partially vacant sites, resulting in a cation–exchange defect. Reproduced with permission.[83] Copyright 2020. American Chemical Society. (e) The crystal structure of disordered spinel $Li_2Sc_{2/3}Cl_4$ from neutron diffraction. Reproduced with permission.[45] Copyright 2020. American Chemical Society. (f) Orthorhombic structure and the $HoCl_6^{3-}$ octahedron of the Li_3HoCl_6 phase. Reproduced with permission.[96] Copyright 2020. American Chemical Society.

ab-plane, thus creating tetrahedral interstitial sites for Li^+ diffusion. Li_3ErCl_6 and Li_3HoCl_6 were isostructural to Li_3YBr_6.[41,89] Li_3BrCl_6 had a monoclinic structure and ccp anion framework. In the ccp anion framework, all the Br atoms were octahedrally coordinated and formed the edge-sharing YBr_6^{3-} and $LiBr_6^{5-}$ octahedra (Fig. 3b).[27,33] Y mostly occupied the 2a site and occupied the 4h site together with Li in the meantime, thus resulting in Li/Y-site disorder. Li was octahedrally coordinated (4g and 4h) and the edge-sharing octahedral arrangement led to multiple tetrahedral voids, where only one was occupied and the others were vacant. Another Li with tetrahedral coordination (8j) was reported later,[90,91] in which $LiBr_4^{3-}$ tetrahedra shared an edge and connected two $LiBr_6^{5-}$ octahedra via a face and simultaneously connected the $LiBr_6^{5-}$ and YBr_6^{3-} octahedra along the (001) plane (Fig. 3c). The chlorides Li_3ScCl_6, Li_3TiCl_6, and Li_3InCl_6 were isostructural to Li_3YBr_6.[24,25,92]

Another monoclinic structure with a $C2/c$ space group was only reported in iodide SSEs.[82,83] The structural framework of Li_3ErI_6 was constructed by edge-sharing ErI_6^{3-} octahedra, in which Er partially occupied 4d and 8f sites. Li^+ was in partially vacant sites and formed the Li/Er-site disorder within layers. Moreover, another Li^+ site (4e) existed in interlayers between the edge-sharing ErI_6^{3-} octahedra and formed an edge-sharing LiI_6^{5-} octahedra layer. These edge-sharing octahedra created tetrahedral vacancies that could provide transitional sites for Li^+ migration (Fig. 3d). In addition, the lithium tetrahaloaluminates $LiAlX_4$ (X = Cl, Br, I) also had a monoclinic structure, but this series of SSEs had limited ionic conductivity.[60,93,94]

Moreover, $Li_2Sc_{2/3}Cl_4$ with an $Fd\bar{3}m$ space group also possessed the ccp anion framework. The halospinel $Li_2Sc_{2/3}Cl_4$ was constructed from edge-sharing $(Sc1/Li4)Cl_6$ octahedra with the remaining Li occupying the face-sharing octahedral (16c) and tetrahedral sites (8a and 48f) (Fig. 3e).[45,79,95] The rigid connectivity of face-sharing octahedra and tetrahedra was more conducive to structural integrity. Both halospinel and monoclinic structures possessed a ccp anion sublattice, and the most important difference was that the Li/metal sites in the halospinel structure were shared, whereas all Li and metal sites were crystallographically ordered in the monoclinic structure.[46] This disordered cation (Li^+ and Sc^{3+}) structure was conducive to Li ion migration.

The orthorhombic structure with a $Pnma$ space group was reported only in Li_3YbCl_6 and Li_3HoCl_6, and the unit cell had 4c, 8d1, and 8d2 octahedral sites. Among them, the Li portion occupied 8d1 and 8d2 sites and M fully occupied the 4c site. Each MX_6^{3-} octahedron was surrounded by three edge-sharing LiM_6^{5-} octahedra (Fig. 3f).[96,97]

Currently, the reported quadrivalent metal chlorides only include Li_2ZrCl_6 and Li_2HfCl_6.[68,86] Li_2ZrCl_6 had two different structures. The one was as-milled Li_2ZrCl_6 and exhibited a trigonal structure, which could be transformed into a monoclinic structure after annealing at 350 °C.[86] The trigonal Li_2ZrCl_6 was isostructural to Li_3YCl_6, and the Li atom preferentially stayed at the 6h site. Another one was the monoclinic Li_2ZrCl_6, which was isostructural to Li_3InCl_6, and had lower occupancy at 2a and 4g sites. Unlike previous cases, the Li_2ZrCl_6 with a trigonal structure and hcp anion sublattice had a higher ionic conductivity than that with a monoclinic structure and ccp anion sublattice (0.81 mS cm^{-1} vs. 5.81 × 10^{-3} mS cm^{-1}). Amounts of nonperiodic features formed in the process of ball

milling promoted Li$^+$ migration in the trigonal structure. For the monoclinic structure, although Li$^+$ migration in the *ab* plane had an energy barrier, the Zr sites effectively hindered Li$^+$ migration between the neighboring *ab* planes, which made it possess two-dimensional (2D) diffusion characteristics. Based on the stochastic surface walking-neural network potential method, Li$_2$ZrCl$_6$ and Li$_2$HfCl$_6$ phases with novel layered structures were designed.[68] This layered Li$_2$ZrCl$_6$ phase was composed of LiCl$_6^{5-}$ and ZrCl$_6^{2-}$ octahedra, which shared the common edges and formed layer-by-layer configuration along the *c*-axis direction. Based on six-coordinating halogen anions with Oct-sites occupied by Zr^{4+} and Li$^+$ cations, the Li$_2$ZrCl$_6$ layered structure contained ideal and Zr-deficient layers with sufficient intrinsic vacancies. This layered structure was quite different from other reports,[85,86] containing more vacancies and defects and giving Li$_2$ZrCl$_6$ more substantial ionic conductivity (~1 mS cm^{-1}).

In addition to hcp and ccp anion sublattices, a high ionic conductivity halide SSE with a non-close-packed anion lattice has recently been reported.[17] This halide SSE was based on LaCl$_3$ with a *P*6$_3$/*m* space group and doped by Ta^{5+} to form a three-dimensional (3D) Li$^+$ diffusion channel to obtain considerable ionic conductivity. In Li$_{0.388}$Ta$_{0.238}$La$_{0.475}$Cl$_3$, Li$^+$ has two sites: a 2b site in channels (Li1) and 6h$_1$ site near La sites (Li2). The former coordinates with 6Cl$^-$ to form a compressed [LiCl$_6$] octahedron. The latter is a metastable intermediate site conducive to the mobility of Li$^+$ and coordinates with adjacent 5Cl$^-$ to form a rectangular pyramid. La^{3+} and Ta^{5+} occupy part of the 2c site together. The key factor for the high ionic conductivity of Li$_{0.388}$Ta$_{0.238}$La$_{0.475}$Cl$_3$ is the abundance of La vacancies formed by Ta^{5+} doping, which connects the one-dimensional (1D) channels in the raw structure into three dimensions.

In both *P*$\bar{3}$*m*1 Li$_3$YCl$_6$ and *C*2/*m* Li$_3$YBr$_6$, the cations (Y^{3+} and Li$^+$) occupied six-coordinated octahedral sites with the halogen anions. Vacancies and Li ion disorders occupied one third of Oct sites, which could facilitate Li ion migration and enable the conductivity of Li$_3$YCl$_6$ and Li$_3$YBr$_6$ to be 0.51 mS cm^{-1} and 1.7 mS cm^{-1}, respectively. It seemed that the ccp sublattice was more favorable for Li ion migration. By adjusting the lattice chemistry of hexagonal Li$_3$YCl$_6$ into a spinel-like cubic structure, a three-dimensional (3D) channel for efficient Li$^+$ transportation could be formed, thus achieving higher ionic conductivity.[98] Park *et al.* calculated 51 structures of 17 chloride electrolytes (Li$_3$MCl$_6$), clearly showing that a monoclinic structure had a lower migration energy barrier and activation energy than orthorhombic and trigonal structures.[99] In orthorhombic and trigonal structures, the sluggish migration of Li$^+$ along the 2D pathway was the main factor for its mediocre ionic conductivity. Among these three space groups of ternary chlorides, the trigonal structure exhibited the highest energy barriers.[99] Besides, a tremendous amount of experimental results also confirmed that the monoclinic structure was more favorable for Li ion diffusion than the orthorhombic structure of halides with the same composition.[38,43,99] This was primarily benefited from the existence of tetrahedral Li$^+$ sites and reasonable 3D ionic migration pathways in monoclinic

structures. The existence of Li ions in tetrahedral sites was favorable for Li ion diffusion.[43] However, Wan and co-workers took the opposite viewpoint, arguing that the ionic conductivity of the trigonal *P*$\bar{3}$*m*1 Li$_3$YCl$_6$ phase was tens of times higher than that of the monoclinic Li$_3$YCl$_6$ phase *C*2/*c* Li$_3$YCl$_6$ phase (10.4 *vs.* 0.69 mS cm^{-1} at 300 K).[71] The results of DFT showed that there were two types of 2D *ab*-plane diffusion paths (Oct–Tet–Oct) with migration barriers of 0.23 and 0.20 eV in the *P*$\bar{3}$*m*1 phase, while there were also other one-dimensional (1D) diffusion paths (Oct–Oct) with a lower barrier (0.16 eV) in the *C*2/*c* phase.

However, the trigonal Li$_2$ZrCl$_6$ exhibits higher ionic conductivity than the monoclinic phase.[85,86] The monoclinic Li$_2$ZrCl$_6$ has a similar crystal structure to Li$_3$InCl$_6$, but the concentration of mobile charge carriers is lower. Furthermore, the ionic radius of Zr^{4+} is smaller than that of In^{3+}, and the stronger coulombic repulsion between Zr^{4+} and Li$^+$ and narrower ion diffusion channel further raise the activation energy barrier for Li$^+$ migration. Therefore, the ionic conductivity of monoclinic Li$_2$ZrCl$_6$ is not as expected. The trigonal Li$_2$ZrCl$_6$ phase is a low-temperature metastable phase with a low crystallinity. The trigonal Li$_2$ZrCl$_6$ has a similar crystal structure to Li$_3$YCl$_6$, and significant amount of nonperiodic features in the crystal structure are key factors for maintaining considerable ionic conductivity. This means the factors affecting the ionic conductivity of halide electrolytes are complex and the crystal structure, carrier concentration, cation radius and defects jointly determine the Li$^+$ migration energy barrier.

Studies on a range of Li$_{3-3x}$M$_{1+x}$Cl$_6$ (M = Tb, Dy, Ho, Y, Er, Tm) with hcp anion stacking showed that the ionic conductivity of the orthorhombic phase was approximately one order of magnitude higher than that of the trigonal phase.[96] According to the AIMD results, the orthorhombic phase had a clear long-range migration pathway along the *z*-axis direction and the hop along the *z*-axis direction had a lower energy barrier than the cross-plane hop. However, the hop was mostly around the hexagon rather than connecting the hexagon in the trigonal phase. The first-principles calculation result of Li$_3$YbCl$_6$ also considered that the orthorhombic structure was superior to the trigonal structure for ionic conductivity.[100]

In brief, halides with a ccp sublattice are more likely to obtain high ionic conductivity, and an orthorhombic structure with a hcp sublattice is more favorable to Li ion migration than a trigonal structure.

2.3 Ionic migration mechanism

Ionic conductivity is easily affected by the ionic diffusion channel and carrier concentration, which were mainly dependent on the crystalline structure, ion spatial array, crystal defect and ion migration mechanism.[84,101,102] The summary of halide SSEs with an ionic conductivity of >0.1 mS cm^{-1} since 2018 is shown in Table 1.

For Li$_3$YCl$_6$ with an hcp-like anion arrangement, there existed two different hop possibilities for transport among connected polyhedra:[27,33,71] (1) the hop along the *c*-axis direction,

Table 1 Summary of halide electrolytes with ionic conductivity greater than 0.1 mS cm^{-1a}

Composition	Structure	Synthesis method	σ [mS cm^{-1}]	Ref.
Li_3YCl_6	Trigonal, $P\bar{3}m1$	BM	0.51	33
Li_3YCl_6	Trigonal, $P\bar{3}m1$	WCS	0.345	63
$Li_{2.5}Y_{0.5}In_{0.5}Cl_6$	Monoclinic, $C2/m$	BM + annealing (260 °C)	1.42	38
$Li_{2.5}Y_{0.5}Zr_{0.5}Cl_6$	Orthorhombic, $Pnma$	SSR (450 °C)	1.4	44
$Li_3YBr_{1.5}Cl_{4.5}$	Trigonal, $P\bar{3}m1$	SSR (650 °C)	2.1	103
$Li_3YBr_3Cl_3$	Monoclinic, $C2/m$	BM + annealing (200 °C)	7.2	104
$Li_3YBr_{4.5}Cl_{1.5}$	Monoclinic, $C2/m$	SSR (650 °C)	5.36	103
Li_3InCl_6	Monoclinic, $C2/m$	WCS	0.79	62
Li_3InCl_6	Monoclinic, $C2/m$	BM + annealing (260 °C)	1.49	25
Li_3InCl_6	Monoclinic, $C2/m$	WCS	2.04	61
$Li_{2.7}In_{0.7}Zr_{0.3}Cl_6$	Monoclinic, $C2/m$	BM + annealing (550 °C)	2.1	105
$Li_{2.7}In_{0.7}Zr_{0.3}Cl_6$	Monoclinic, $C2/m$	SSR (450 °C)	2.02	106
$Li_{2.6}In_{0.6}Zr_{0.4}Cl_6$	Monoclinic, $C2/m$	BM + annealing (260 °C)	1.25	107
$Li_{2.75}In_{0.75}Zr_{0.25}Cl_6$	Monoclinic, $C2/m$	BM + annealing (450 °C)	5.82	108
$Li_{2.9}In_{0.9}Zr_{0.1}Cl_6$	Monoclinic, $C2/m$	BM + annealing (260 °C)	1.54	109
$Li_{2.7}In_{0.7}Hf_{0.3}Cl_6$	Monoclinic, $C2/m$	BM + annealing (350 °C)	1.28	88
$Li_2In_{0.444}Sc_{0.222}Cl_4$	Spine, $Fd\bar{3}m$	BM + annealing (450 °C)	2.03	46
$Li_3InCl_{4.8}F_{1.2}$	Monoclinic, $C2/m$	BM + annealing (260 °C)	0.51	110
$Li_3InCl_{5.6}F_{0.4}$	Monoclinic, $C2/m$	BM + annealing (300 °C)	1.37	111
Li_3ErCl_6	Trigonal, $P\bar{3}m1$	BM + annealing (550 °C)	0.3	40
Li_3ErCl_6	Trigonal, $P\bar{3}m1$	WCS	0.407	63
Li_3ErCl_6	Trigonal, $P\bar{3}m1$	BM	0.33	41
Li_3ErCl_6	Trigonal, $P\bar{3}m1$	BM + annealing (550 °C)	0.1	41
$Li_{2.6}Er_{0.6}Zr_{0.4}Cl_6$	Trigonal, $P\bar{3}m1$	BM	1.38	39
$Li_{2.633}Er_{0.633}Zr_{0.367}Cl_6$	Orthorhombic, $Pnma$	SSR (450 °C)	1.1	44
Li_3YbCl_6	Trigonal, $P\bar{3}m1$	BM + annealing (400 °C)	0.19	43
Li_3YbCl_6	Orthorhombic, $Pnma$	BM + annealing (500 °C)	0.14	43
$Li_{2.556}Yb_{0.492}Zr_{0.492}Cl_6$	Orthorhombic, $Pnma$	SSR (450 °C)	1.58	100
$Li_{2.7}Yb_{0.7}Hf_{0.3}Cl_6$	Orthorhombic, $Pnma$	BM + annealing (350 °C)	1.1	97
$Li_{2.6}Yb_{0.6}Hf_{0.4}Cl_6$	Monoclinic, $C2/m$	BM + annealing (400 °C)	1.5	43
$Li_{2.6}Yb_{0.6}Hf_{0.4}Cl_6$	Orthorhombic, $Pnma$	BM + annealing (500 °C)	1.2	43
Li_3TiCl_6	Monoclinic, $C2/m$	BM	0.115	92
Li_3TiCl_6	Monoclinic, $C2/m$	BM + annealing (300 °C)	1.04	92
Li_2ZrCl_6	Trigonal, $P\bar{3}m1$	BM	0.4	85
$Li_{2.25}Zr_{0.75}Fe_{0.25}Cl_6$	Trigonal, $P\bar{3}m1$	BM	0.98	85
$Li_{2.25}Zr_{0.75}V_{0.25}Cl_6$	Trigonal, $P\bar{3}m1$	BM	~0.9	85
$Li_{2.1}Zr_{0.9}Cr_{0.1}Cl_6$	Trigonal, $P\bar{3}m1$	BM	~0.85	85
$Li_{2.25}Zr_{0.75}In_{0.25}Cl_6$	Trigonal, $P\bar{3}m1$	BM	1.08	112
$Li_{2.1}Zr_{0.95}Mg_{0.05}Cl_6$	Trigonal, $P\bar{3}m1$	BM	0.62	113
$ZrO_2-2LiCl-Li_2ZrCl_6$	Trigonal, $P\bar{3}m1$	BM + annealing (550 °C)	1.3	114
Li_2ZrCl_6	Layered structure	BM	~1.0	68
Li_2HfCl_6	Layered structure	BM	~0.5	68
Li_3HoCl_6	Trigonal, $P\bar{3}m1$	SSR	1.05	89
$Li_{2.73}Ho_{1.09}Cl_6$	Trigonal, $P\bar{3}m1$	SSR (650 °C)	1.3	96
$Li_2Sc_{2/3}Cl_4$	Spine, $Fd\bar{3}m$	SSR (680 °C)	1.5	45
Li_3ScCl_6	Monoclinic, $C2/m$	SSR (650 °C)	3.02	24
Li_3ScCl_6	Monoclinic, $C2/m$	WCS	1.25	63
$Li_{2.5}Sc_{0.5}Zr_{0.5}Cl_6$	Monoclinic, $C2/m$	SSR (500 °C)	2.23	115
$Li_{2.6}Sc_{0.6}Zr_{0.4}Cl_6$	Monoclinic, $C2/m$	BM + annealing (450 °C)	1.61	116
$Li_{2.6}Sc_{0.6}Hf_{0.4}Cl_6$	Monoclinic, $C2/m$	BM + annealing (450 °C)	1.33	116
$LiTaCl_6$	Glass-phase	BM + annealing (120 °C)	10.95	117
Li_3YBr_6	Monoclinic, $C2/m$	BM + annealing (550 °C)	1.7	33
Li_3YBr_6	Monoclinic, $C2/m$	WCS	1.09	63
$Li_3YBr_{5.7}F_{0.3}$	Monoclinic, $C2/m$	SSR (950 °C)	1.8	118
Li_3HoBr_6	Monoclinic, $C12/m1$	SSR (450 °C)	1.1	119
Li_3HoBr_6	Monoclinic, $C12/m1$	WCS	1.25	120
$Li_3HoBr_{2.9}I_{3.1}$	Monoclinic, $C2/m$	SSR (1000 °C)	2.7	121
Li_3ErI_6	Monoclinic, $C2/c$	BM	0.65	83
Li_3ErI_6	Monoclinic, $C2/c$	BM + annealing (550 °C)	0.39	83

^{a} BM: ball milling; SSR: solid state reaction; WCS: wet-chemistry synthesis.

where the pathway was directly connected between adjacent octahedral sites (Oct–Oct) and had a low energy barrier of 0.25 eV and (2) the hop in the *ab*-plane, where the pathway was *via* tetrahedral interstitial sites (Oct–Tet–Oct) and exhibited an energy barrier of 0.29 eV (Fig. 4a). The ionic conductivities along the *c*-, *a*-, and *b*-axis in Li_3YCl_6 were 85.4, 0.3, and 0.7 mS cm^{-1}, respectively.[122] It could be seen that Li$^+$ diffusion in Li_3YCl_6 was highly anisotropic and had a fast *c*-axis 1D diffusion channel. Such anisotropic diffusion made the conductivity extremely susceptible to channel-blocking defects, including anti-site defects, impurities, and grain boundaries, which caused ionic conductivity to deviate significantly from theoretical prediction. For Li_3YBr_6 with a ccp anion arrangement, the Li$^+$ conducting pathway showed a 3D isotropic network and Li$^+$ hopped to the adjacent octahedral site through a tetrahedral interstitial site (Oct–Tet–Oct pathway), thereby exhibiting a barrier of 0.28 eV (Fig. 4b).[27] Further AIMD results showed that the 3D isotropic diffusion pathway was based on two channels: the hopping between different Li-1 sites in the (001) plane, and the activation energy was between 0.11 and 0.19 eV; the hopping between Li-1 and Li-2 sites along the [001] direction, and the activation energy was 0.39 eV.[123]

The ion migration of Li_3ErI_6 with a monoclinic structure was mainly 2D in the *ab*-plane (Fig. 4c). In the *ab*-plane, Li sites were strongly interconnected with each other, and the tetrahedral voids left by the edge-sharing of octahedra were used as transition sites for Li$^+$ diffusion. Of course, the strong disorder between Li$^+$ and Er^{3+} indicated the possibility of Li$^+$ migration

along the *c*-axis direction. Based on DFT calculations, monoclinic Li_3HoBr_6 had four possible diffusion pathways.[119] The vacancies in the lattice provided different pathways for Li ion diffusion. The energy barriers of these two in-plane pathways were 0.22 eV and 0.46 eV for Oct–V$_{Oct}$ and Oct–Oct pathways, respectively. In addition, the energy barriers for two out-of-plane paths were 0.12 eV and 0.24 eV for Oct–Tet–V$_{Oct}$ and Oct–Tet–Oct pathways, respectively. In contrast, Li ions showed a lower energy barrier to migrate through vacant octahedral sites. However, the number of such natural vacant octahedral sites was limited and couldn't fully supply Li ion migration. The Oct–Tet–Oct pathway in the out-of-plane could be used as a complementary contribution to Li ion migration. The synergistic effect of multiple diffusion pathways with low activation barriers in Li_3HoBr_6 well guaranteed the high ionic conductivity.

The high ionic conductivity of $Li_2Sc_{2/3}Cl_4$ was mainly due to multiple Li sites in the spinel lattice. The rigid framework formed by the Li/Sc shared site and the presence of Li$^+$ throughout the face-sharing octahedral and tetrahedral sites, provided the conditions for infinite 3D Li$^+$ diffusion pathways (Fig. 4d). In addition, the large number of vacancies formed by the Li deficiency strategy was beneficial in eliminating the defect formation step for Li$^+$ diffusion.[45] $Li_2Sc_{2/3}Cl_4$ prepared by a facile synthesis process exhibited an ionic conductivity of 1.5 mS cm^{-1}. The results of DFT showed that halospinel $Li_2Sc_{2/3}Cl_4$ had the potential for ionic conductivity of up to ~2.07 mS cm^{-1} under a collective ionic motion mechanism.[79] Before the first Li
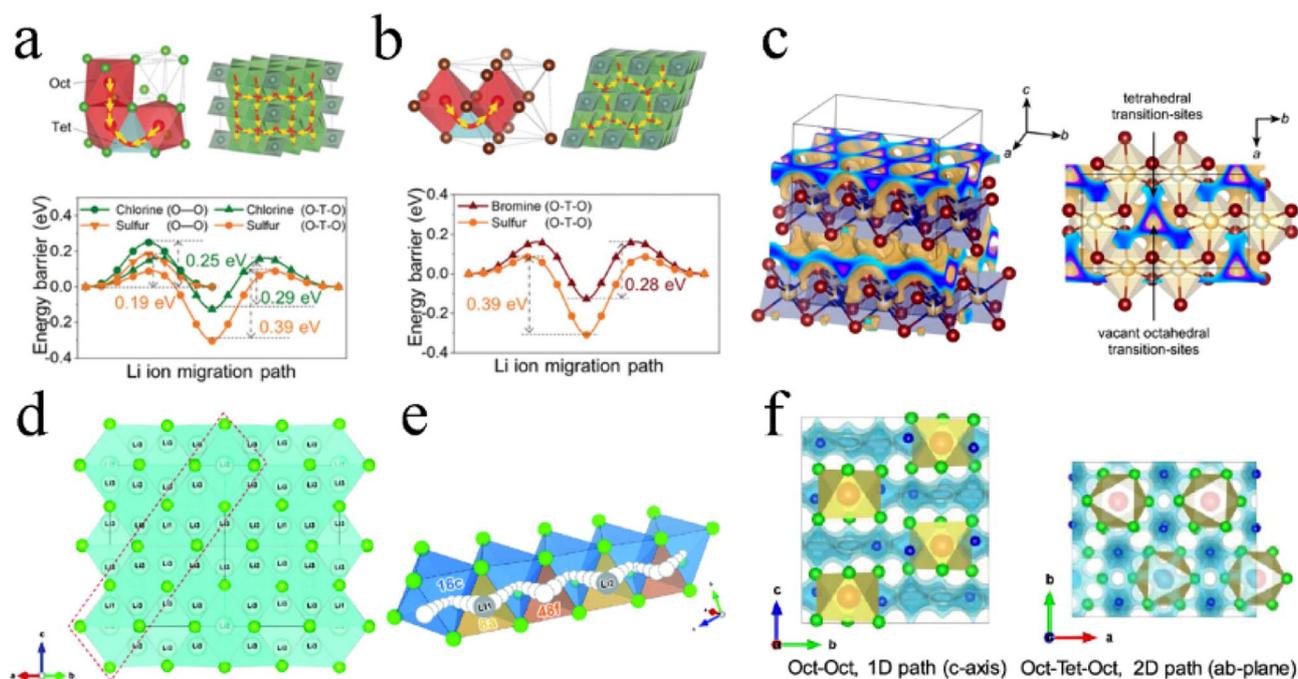
Fig. 4 The Li$^+$ migration pathways and corresponding energy landscape in (a) Li_3YCl_6 and (b) Li_3YBr_6. Reproduced with permission.[27] Copyright 2019, Wiley-VCH. (c) Possible Li$^+$ diffusion pathways of Li_3ErI_6 obtained by a bond valence sum calculation. Reproduced with permission.[83] Copyright 2020. American Chemical Society. (d) Structure and 3D Li$^+$ diffusion pathway of disordered spinel $Li_2Sc_{2/3}Cl_4$. Reproduced with permission.[45] Copyright 2020. The Royal Society of Chemistry. (e) Schematic diagram of collective Li$^+$ motion. Reproduced with permission.[79] Copyright 2020. The Royal Society of Chemistry. (f) Li$^+$ migration pathway in orthorhombic Li_3MCl_6 obtained by the BVSE method. Reproduced with permission.[99] Copyright 2020. American Chemical Society.

(Li1) at the 8a site hopped to the 48f site, the strong Coulomb repulsion between Li1 and Li2 drove Li2 to jump to the next 48f site, followed by Li1 hopping to the 8a site, where Li2 was initially located. Hence, rapid Li^+ migration was achieved repeatedly (Fig. 4e).

The orthorhombic structure was similar to the trigonal structure and exhibited the anisotropic diffusion pathways of Li ions (Fig. 4f): 1D diffusion pathway along the c-axis direction between the octahedral sites (Oct–Oct pathway) with lower activation energy and 2D diffusion pathway in the ab-plane between octahedral sites and interstitial tetrahedral sites (Oct–Tet–Oct pathway) with higher activation energy.

The site disorder in the crystal structure had a direct influence on the ion diffusion pathway of halide SSEs. At present, researchers don't have a unified understanding of the relevant mechanism. Experimental studies on Li_3YCl_6 and Li_3ErCl_6 showed that higher cationic site disorder was favorable to ion transport.[33,40,41] The disordered and distorted structure expanded the bottleneck of Li^+ diffusion and significantly affected the transport mechanism. Consistent with this result, the stacking faults in Li_3YCl_6 could reduce the Li^+ migration barrier and generate more interlayer channels, thereby promoting Li^+ conduction in the structure.[124] In contrast, theoretical work suggested that antisite disorder blocked the Li^+ diffusion channel and reduced conductivity by about one order of magnitude.[25] Calculation results by Wan *et al.* showed that antisite defects formed in Li_3YCl_6 were favorable for converting the $P\bar{3}m1$ lattice to the $C2/c$ lattice with low ionic conductivity and limiting Li^+ transportation.[71]

3. Substitution in halide SSEs

Chemical substitution in known ionic conductors was often used to develop new electrolytes with improved ionic conductivity, electrochemical/chemical stability, and environmental stability.[35,125,126]

3.1 Haloanion substitution

Fluoride exhibited a wider electrochemical stability window, while chloride and bromide had more prominent ionic conductivity. Therefore, dual-halogen SSEs were formed by haloanion substitution, which could balance oxidative stability and ionic conductivity and obtain better comprehensive performance. The introduction of Cl^- into $Li_2ZrF_{6-x}Cl_x$ could maintain the excellent Li interface stability, meanwhile improving ionic conductivity by two orders of magnitude.[127] Compared with other halide anions, F^- had the smallest ionic radius. Therefore, F^- substitution usually led to lattice shrinkage.[110,111,118,128] F^- had shorter and stronger bonds with Li^+ in comparison with Cl^-, increasing the barrier for Li^+ migration. And the conductivity of chloride decreased slightly after F^- doping.[71] In F-doped $Li_3InCl_{4.8}F_{1.2}$, Cl occupied symmetrical 4i and 8j sites and F occupied partial 8j sites. Cl and F were stacked layer-by-layer to form an edge-share six-coordinated octahedron, and the cation and vacancy occupied octahedral interstitial sites (Fig. 5a).[110] The experimental results showed that the ionic conductivity of $Li_3InCl_{6-x}F_x$ gradually decreased with the F content increasing (Fig. 5b).[111] However, according to the first-principles theoretical method, the
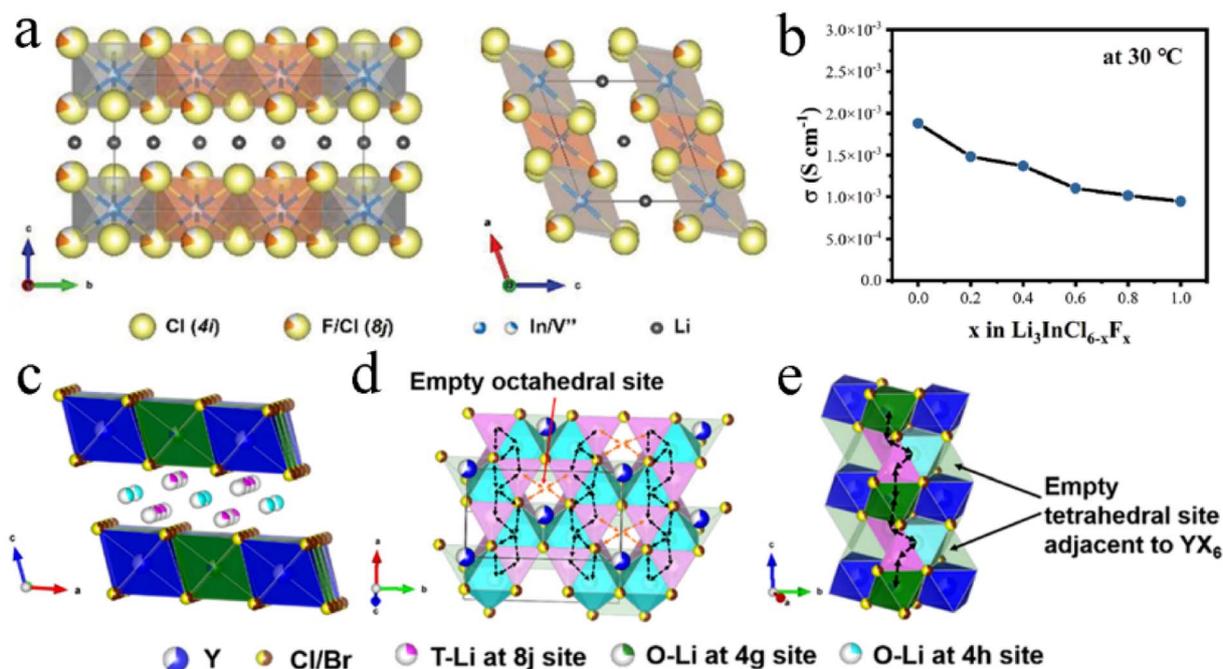
Fig. 5 (a) Crystal structure of $Li_3InCl_{4.8}F_{1.2}$ viewed from different orientations. Reproduced with permission.[110] Copyright 2021, Wiley-VCH. (b) Ionic conductivity of $Li_3InCl_{6-x}F_x$ with different F-contents at room temperature. Reproduced with permission.[111] Copyright 2022. Elsevier B.V. (c) Crystal structure of $Li_3Y(Br_3Cl_3)$ viewed from parallel to the a-axis. Reproduced with permission.[104] Copyright 2020. American Chemical Society. Migration routes of Li ions along the (d) ab-plane and (e) c-axis direction. Reproduced with permission.[104] Copyright 2020. American Chemical Society.

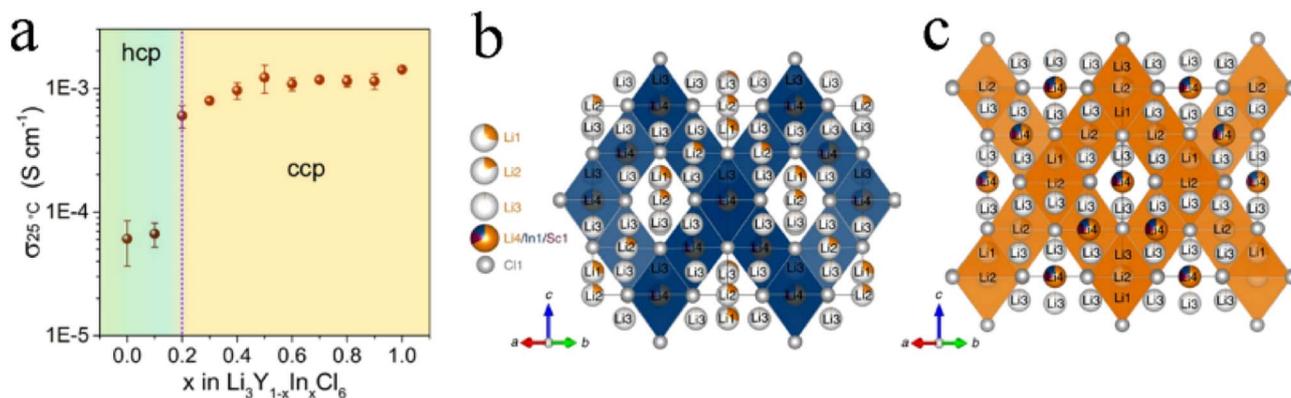**Fig. 6** (a) Ionic conductivity of $Li_3Y_{1-x}In_xCl_6$ with different In contents at 25 °C. Reproduced with permission.[38] Copyright 2020, American Chemical Society. Structure (b) and the main 3D Li ion diffusion pathway (c) of $Li_2In_{1/3}Sc_{1/3}Cl_4$. Reproduced with permission.[46] Copyright 2022, Springer Nature.

changed from halospinel to monoclinic.[46] The spinel $Li_2In_{1/3}Sc_{1/3}Cl_4$ was constructed from the edge-sharing (In1/Sc1/Li4) Cl_6 octahedral rigid framework, while the additional Li^+ spread throughout face-sharing octahedral and tetrahedral sites (Fig. 6b). The low occupancy of face-sharing octahedral and tetrahedral sites provided a considerable number of vacancies for Li^+ mobility, which could form 3D ion diffusion channels with relatively low activation energy and obtain an ionic conductivity of more than 2 mS cm^{-1} (Fig. 6c).

3.3 Aliovalent cation substitution

An aliovalent substitution could significantly affect the ionic conductivity and activation energy, due to providing more free

interstitial sites, increasing the number of charge carriers, and broadening diffusion pathways.

Tetravalent Zr^{4+} and Hf^{4+} were usually doped into trivalent metal halides as aliovalent ions.[39,44,88,97,106-108] The introduction of Zr^{4+} into Li_3YCl_6 and Li_3ErCl_6 by a solid-state reaction at 450 °C resulted in crystal structure changes.[44] As Zr content increased, their crystal structure changed from the trigonal structure, first to an orthorhombic-I structure and then to an orthorhombic-II structure (Fig. 7a). The former phase transformation process involved the rearrangement of metal ions, and the latter one only led to the occurrence of the tilt for (Er/Zr)Cl_6 octahedra and created an additional tetrahedral Li site. Compared with the other two crystal structures, the
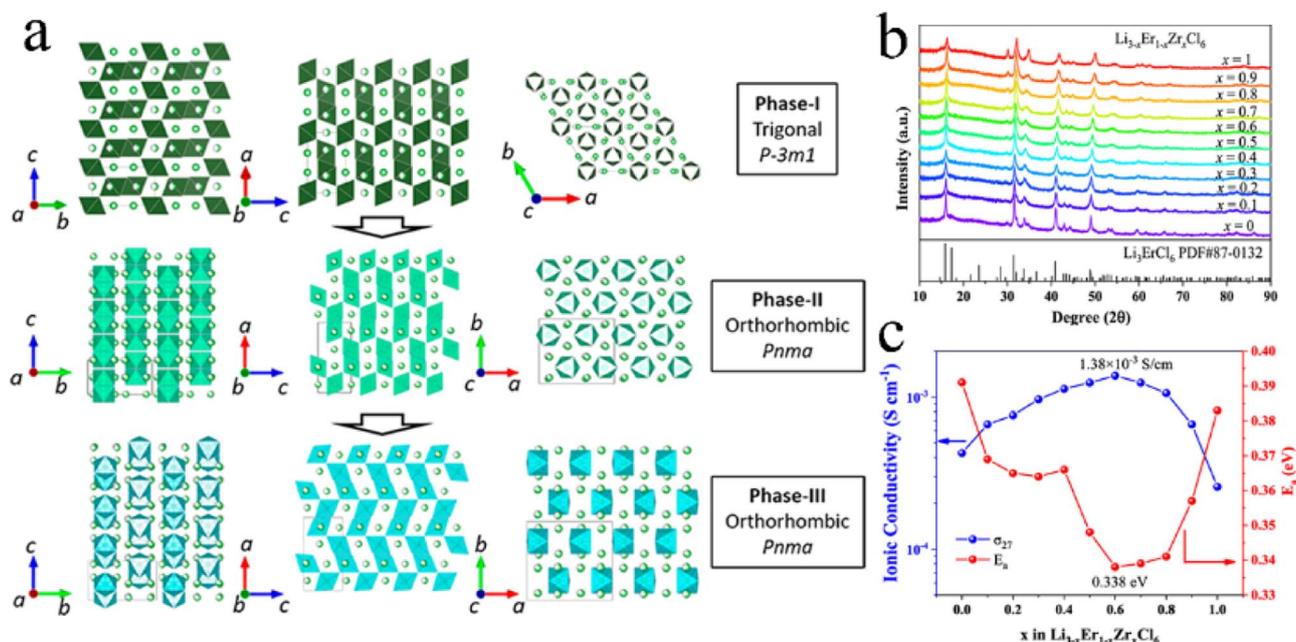
Fig. 7 (a) Phase evolution of $Li_3M_{1-x}Zr_xCl_6$ (M = Er, Y) upon Zr substitution. Reproduced with permission.[44] Copyright 2020, American Chemical Society. (b) XRD patterns of $Li_{3-x}Er_{1-x}Zr_xCl$ (x = 0-1) obtained from ball-milling. Reproduced with permission.[39] Copyright 2022. American Chemical Society. (c) Ionic conductivity and activation energy for $Li_{3-x}Er_{1-x}Zr_xCl$ as a function of x. Reproduced with permission.[39] Copyright 2022. American Chemical Society.

orthorhombic-II structure had obvious advantages in ionic conductivity. The ionic conductivities of $Li_{2.633}Er_{0.633}Zr_{0.367}Cl_6$ and $Li_{2.5}Y_{0.5}Zr_{0.5}Cl_6$ with the orthorhombic-II structure were 1.1 and 1.4 mS cm^{-1}, respectively. However, another report was against this viewpoint that Zr-doping caused phase transitions.[39] $Li_{3-x}Er_{1-x}Zr_xCl_6$ prepared by ball-milling had the same trigonal structure as Li_3ErCl_6 regardless of the Zr content (Fig. 7b). And this structure didn't change during annealing. The ionic conductivity of ball-milled $Li_{3-x}Er_{1-x}Zr_xCl_6$ first increased and then decreased with an increase in Zr content, where the maximum value reached 1.38 mS cm^{-1} at $x = 0.6$ (Fig. 7c). On the one hand, the appropriate Zr^{4+} substitution increased the concentration of Li vacancies and Er/Zr site disorder, facilitating the increase in ionic conductivity. On the

other hand, excessive Zr^{4+} substitution reduced the concentration of Li^+ and then caused lattice shrinkage and narrowed the transport channel of Li^+, thus impeding the migration of Li^+. The AIMD results also showed that replacing Y^{3+} with Zr^{4+} in Li_3YCl_6 could not only increase the Li vacancy concentration through charge compensation, but also increase the Coulomb force between Li and immobile ions, thus limiting the migration of Li^+.[71]

In addition to the size of doped metal ions, the heat treatment scheme was also a key factor in phase transformation. For Li_3YbCl_6, the orthorhombic phase was stable, while the metastable trigonal phase was formed when the solid state reaction or annealing was performed at low temperature.[43,97] The appropriate aliovalent cation substitution (Zr^{4+} or Hf^{4+}) for Yb^{3+}

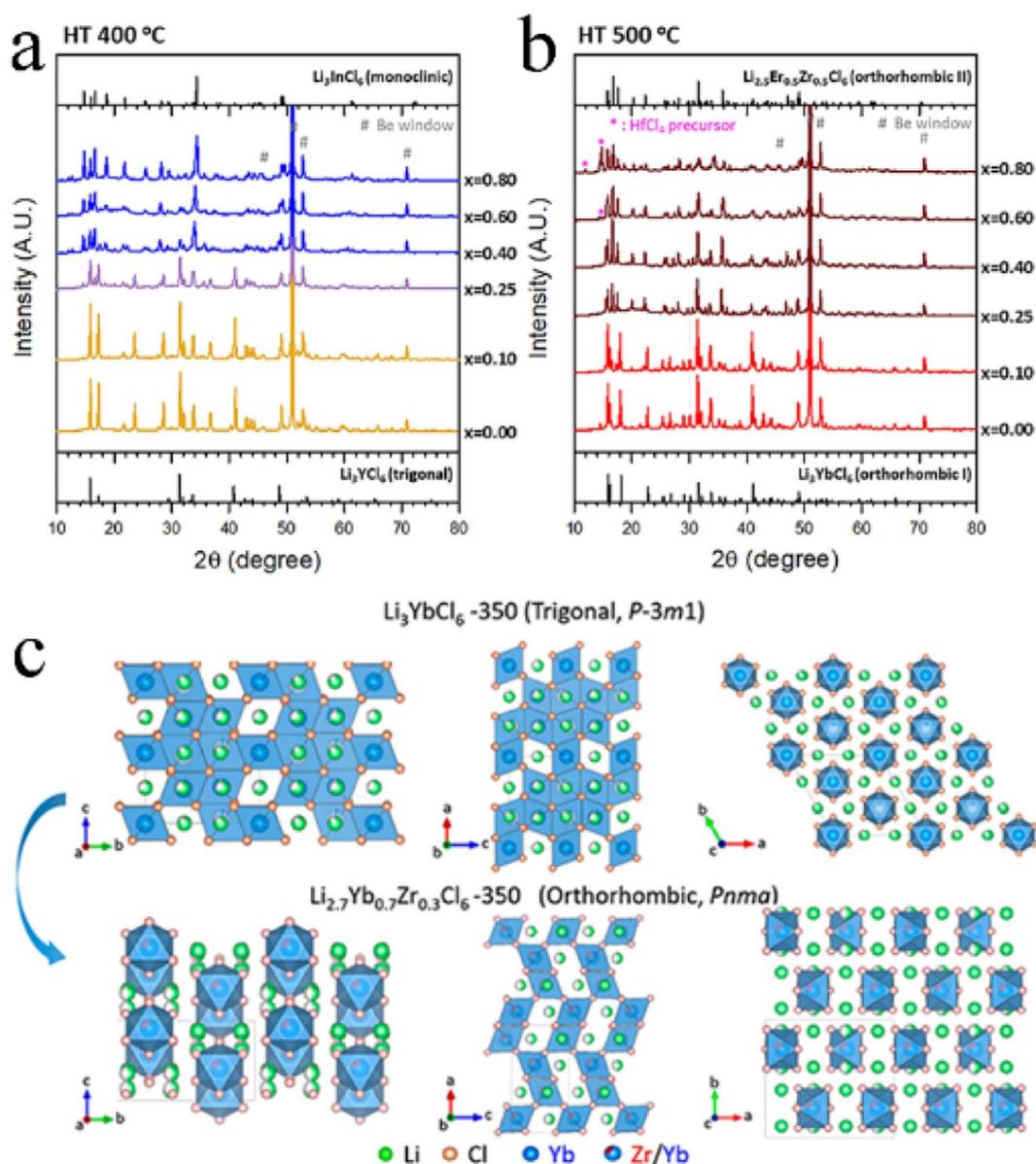**Fig. 8** XRD patterns of $Li_{3-x}Yb_{1-x}Hf_xCl_6$ annealed at (a) 400 °C and (b) 500 °C. Reproduced with permission.[43] Copyright 2021. Elsevier B.V. (c) Structural evolution of Li_3YbCl_6-350 to $Li_{2.7}Yb_{0.7}Zr_{0.3}Cl_6$-350 by Zr substitution. Reproduced with permission.[97] Copyright 2021. American Chemical Society.

in Li_3YbCl_6 triggered the phase transition, whether it was a metastable trigonal phase or stable orthorhombic phase. With the increase in Hf content, the crystal structure of $Li_{3-x}Yb_{1-x}Hf_xCl_6$ prepared by mechanochemical synthesis could change from a trigonal structure to a monoclinic structure when annealed at 400 °C (Fig. 8a), and from the original orthorhombic-I structure to an orthorhombic-II structure when annealed at 500 °C (Fig. 8b). Their ionic conductivity also showed a parabolic trend of reaching a peak value of 1.5 and 1.2 mS cm^{-1} at $x = 0.4$ with the increase in Hf content, respectively.[43] The effect of substitution on ionic conductivity derived from the combination of phase transition and the concentration of charge carriers of ions or Li vacancies.[43] With the increase in Zr content, the crystal structure of $Li_{3-x}Yb_{1-x}Zr_xCl_6$ synthesized by a solid state reaction at 350 °C changed from a trigonal structure to an orthorhombic structure (Fig. 8c).[97] The phase transition triggered metal ion rearrangement and then generated an interstitial tetrahedral site between Li1 and Li2 sites, which provided an intermediate "stepping stone" for Li$^+$ migration. The 1D Li$^+$ migration pathway through the face sharing Li1 and Li2 octahedral sites along the c-axis path was expanded to a 3D network. The ionic conductivity of orthorhombic $Li_{2.7}Yb_{0.7}Zr_{0.3}Cl_6$ was improved by nearly ten times compared with that of trigonal Li_3YbCl_6, reaching 1.1 mS cm^{-1}. After further optimization, the ionic conductivity of $Li_{2.556}Yb_{0.492}Zr_{0.492}Cl_6$ reached up to 1.58 mS cm^{-1}.[100]

Replacing In^{3+} with different amounts of Zr^{4+} or Hf^{4+} in Li_3InCl_6 could still maintain a monoclinic structure.[88,106–109] In $Li_{3-x}In_{1-x}Zr_xCl_6$, the Zr^{4+} only occupied the 2b site (Fig. 9a) and the occupancy of In at the 4g site gradually decreased with the Zr content increasing. It was noteworthy that the occupancy of tetrahedral Li3 (8j) sites almost linearly decreased with the increase in Zr content, until complete disappearance.[106,107] Li_3InCl_6 had two possible Li$^+$ diffusion pathways: one was along the c-direction, involving the octahedral 2c site, tetrahedral 8j site, and shared octahedral 4g site. The other was along the Li-layer in the ab-plane, involving both the octahedral Li-sites in the layer and the vacant tetrahedra. The contribution ratio of the former and the latter to ionic conductivity was about 1:10. After the introduction of Zr^{4+}, In^{3+} and Zr^{4+} occupied the octahedral site in large quantities, hindered the diffusion of Li$^+$ in the mixed cation layer, and then reduced the possibility of long-range diffusion. The Oct–Tet–Oct pathway along the c-axis was also blocked by the high cumulative occupancy of the In2/Li4 site. At the same time, Zr^{4+} substitution led to a decrease in In occupation at the 4g site, and Li was removed from the tetrahedral site under charge compensation, thus opening up a new diffusion pathway along the c-axis (Fig. 9b). Moreover, Zr^{4+} substitution changed the preferred orientation of Li_3InCl_6 from the (001) plane to the (131) plane, which might be conducive to the construction of 3D Li$^+$ migration channels. The Zr^{4+} substitution strategy made the ionic conductivity of $Li_{2.9}In_{0.9}Zr_{0.1}Cl_6$ significantly increase to 1.54 mS cm^{-1}, which was nearly double that of Li_3InCl_6.[109] The research of van der Maas et al. on a series of $Li_{3-x}In_{1-x}Zr_xCl_6$ showed that the conductivity reached a maximum value of 2.02 mS cm^{-1}, when $x =$
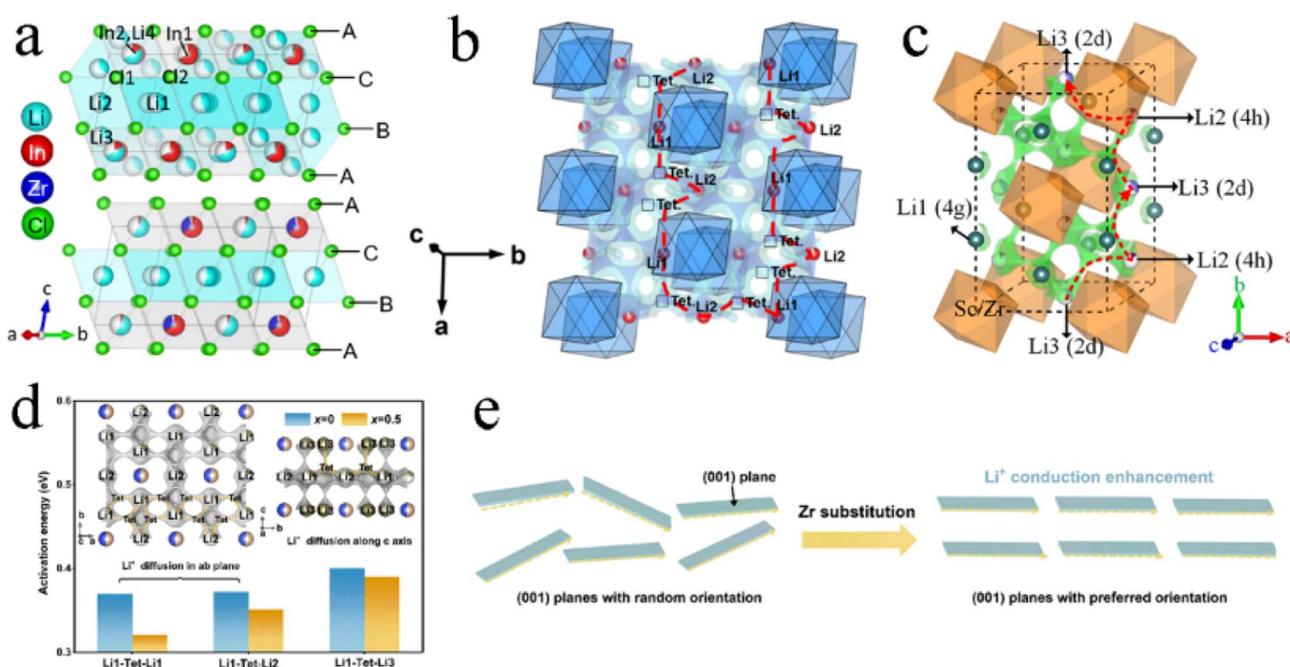
Fig. 9 (a) The structure of Li_3InCl_6 (upper) and $Li_{2.7}In_{0.7}Zr_{0.3}Cl_6$ (below). Reproduced with permission.[106] Copyright 2023, The Royal Society of Chemistry. (b) Migration pathways of $Li_{3-x}In_{1-x}Hf_xCl_6$ along the a-axis direction. Reproduced with permission.[88] Copyright 2023, American Chemical Society. (c) The Li$^+$ migration pathways of $Li_{3-x}Sc_{1-x}Zr_xCl_6$ marked with the green isosurfaces, and one of the migration pathways is highlighted with a red dotted line with arrows. Reproduced with permission.[116] Copyright 2023, Wiley-VCH. (d) Comparison of the energy barrier values for Li$^+$ migration through different pathways in Li_3ScCl_6 and $Li_{2.5}Sc_{0.5}Zr_{0.5}Cl_6$. Reproduced with permission.[115] Copyright 2022, Elsevier B.V. (e) Schematic illustration of Li$^+$ conduction in (001) planes with a randomly distributed orientation and preferred orientation. Reproduced with permission.[115] Copyright 2022, Elsevier B.V.

$0.3.$[106] However, Helm recognized that conductivity peaks at 1.2 mS cm^{-1} when $x = 0.4$.[107] This remarkable difference might be due to the different methods of preparing $Li_{3-x}In_{1-x}Zr_xCl_6$. Based on the AIMD modeling results, the ionic conductivity of $Li_{2.75}In_{0.75}Zr_{0.25}Cl_6$ synthesized by Fu *et al.* could reach as high as 5.82 mS cm^{-1}.[108] The mechanism of tetravalent Hf^{4+} substitution on $Li_{3-x}In_{1-x}Hf_xCl_6$ was analogous to that of Zr^{4+}, which improved ionic conductivity by forming interstitial tetrahedral sites and Li vacancies.[88] At $x = 0.3$, the ionic conductivity of $Li_{2.7}In_{0.7}Hf_{0.3}Cl_6$ reached a maximum of 1.54 mS cm^{-1}.

Similarly, introducing Zr^{4+} or Hf^{4+} into Li_3ScCl_6 didn't change the monoclinic structure.[115,116] Zr^{4+}/Hf^{4+} was randomly located at the Sc^{3+} 2a site, resulting in local structural distortion due to the difference in ion radii. The partially occupied Li2- and Li3-centered octahedra expanded, while the fully occupied Li1-centered octahedra shrank. The former could weaken the restriction of surrounding Cl^-, thus promoting the migration of Li ions. This substitution couldn't change the 2D diffusion pathway of Li^+ in the Li2/Li3-plane, which used tetrahedral interspaces as an intermediary site (Fig. 9c). Since Zr^{4+} and Hf^{4+} had a higher valence than Sc^{3+}, they exhibited a stronger coulombic repulsion with Li^+, thus well stabilizing the 2D diffusion path in the Li2/Li3-plane by limiting the random diffusion of Li ions. The resulting ionic conductivity was 1.61 and 1.33 mS cm^{-1} for $Li_{2.6}Sc_{0.6}Zr_{0.4}Cl_6$ and $Li_{2.6}Sc_{0.6}Hf_{0.4}Cl_6$ respectively, which were much higher than that of Li_3ScCl_6 (0.6 mS cm^{-1}).[116] Li *et al.* thought that both Li_3ScCl_6 and

$Li_{3-x}Sc_{1-x}Zr_xCl_6$ had a 3D Li^+ diffusive channel.[115] The migration energy barriers of pathways in the *ab* plane were lower than those along the *c*-axis, and the migration of Li^+ was still dominated by the *ab* plane pathway (Fig. 9d). The substitution of Sc^{3+} by Zr^{4+} reduced the migration energy barriers in this pathway. In addition, the Zr^{4+} substitution increased the concentration of Li vacancies. Most surprisingly, the Zr^{4+} substitution could improve the degree of preferred orientation in (001) planes (Fig. 9e). This structure reduced Li^+ migration resistance along each *ab* plane and between contiguous *ab* planes and enabled Li^+ to hop rapidly along the parallelly aligned *ab* planes with small misorientation, thus improving the ionic conductivity. $Li_{2.5}Sc_{0.5}Zr_{0.5}Cl_6$ exhibited an ionic conductivity of up to 2.23 mS cm^{-1}, which was 3.28-fold higher than that of pristine Li_3ScCl_6.[115]

Li_2ZrCl_6 had a metastable trigonal structure and stable monoclinic structure, and the trivalent metal ions (In^{3+}, Sc^{3+}, and Fe^{3+}) exhibited different substitution effects on these two structures. All $Li_{2+x}Zr_{1-x}In_xCl_6$ ($0 \leq x \leq 1.0$) annealed at 260 °C after ball milling were of monoclinic phase with a space group of $C2/m$, and doping In^{3+} didn't change the crystal structure.[105] As the content of In^{3+} increased, the lattice of $Li_{2+x}Zr_{1-x}In_xCl_6$ expanded asymmetrically and the $ZrCl_6^{2-}$ octahedra distorted. The introduced In^{3+} initially occupied the 2a site and gradually occupied the 4g site when x exceeded 0.6, resulting in the disappearance of Zr^{4+} at that site. In unsubstituted Li_2ZrCl_6, Li^+ preferred to present at the M2/Li3 site in the (001) plane rather
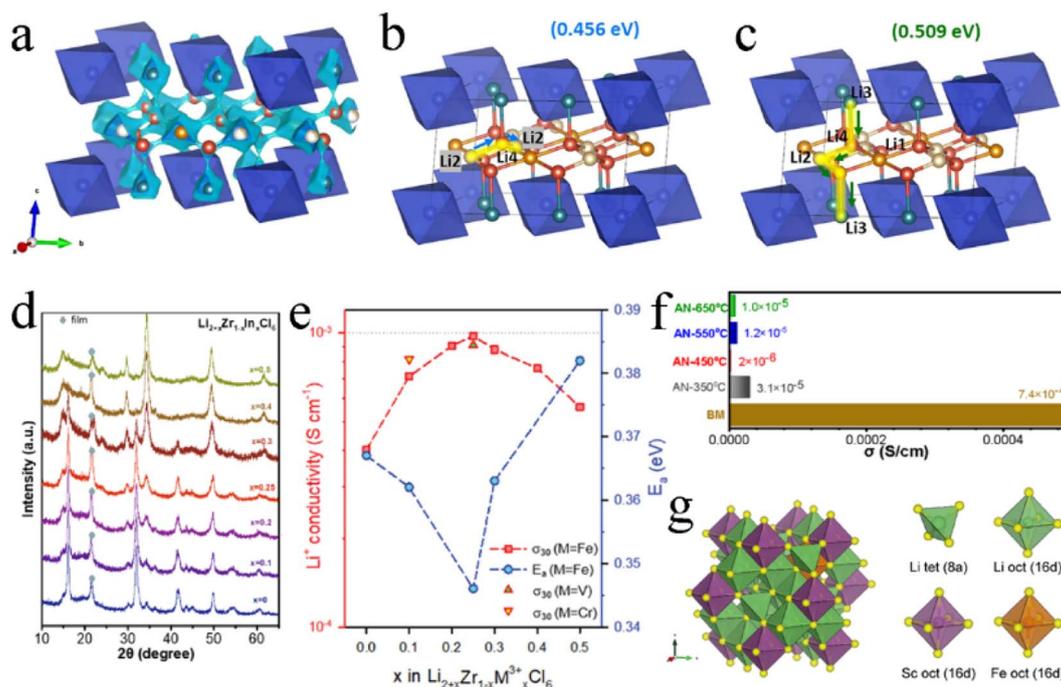
Fig. 10 (a) Li^+ diffusion pathways of $Li_{2+x}Zr_{1-x}In_xCl_6$ with an iso-surface value of ± 0.5 v.u. Reproduced with permission.[105] Copyright 2022, Elsevier B.V. Possible Li^+ conduction pathways in the *ab*-plane (b) and along the *c*-axis (c). Reproduced with permission.[105] Copyright 2022, Elsevier B.V. (d) XRD patterns of $Li_{2+x}Zr_{1-x}In_xCl_6$. Reproduced with permission.[112] Copyright 2022, Elsevier B.V. (e) Ionic conductivity at 30 °C and activation energy for $Fe^{3+}/V^{3+}/Cr^{3+}$-substituted Li_2ZrCl_6. Reproduced with permission.[85] Copyright 2021, Wiley-VCH. (f) Comparison of ionic conductivity between ball-milled and annealed $Li_{2.25}Zr_{0.75}Fe_{0.25}Cl_6$ electrolytes. Reproduced with permission.[129] Copyright 2022, Elsevier B.V. (g) The most thermodynamically stable structure of $Li_2S_{2/3}Cl_4-0.2Fe$ and its components. Reproduced with permission.[95] Copyright 2023, The Royal Society of Chemistry.

than Li1, Li2, and Li4 sites in the (002) plane. The introduction of In^{3+} enabled the occupancy of the Li3 site to be decreased and enabled the occupancy of L1 and L2 sites to be increased upon substitution. Even when x was greater than 0.4, the Li4 site was occupied. This played a key role in improving ionic conductivity. The Li4 site was conducive not only to the intra-layer Li^+ diffusion in the ab-plane, but also to the interlayer Li^+ diffusion along the c-axis, which was the basis of the 3D diffusion pathway (Fig. 10a–c). In addition, the substitution of In^{3+} made the concentration of Li^+ more abundant and expanded the anisotropic lattice, and the Li^+ redistribution in the lattice also made the energy landscape more favorable for Li^+ migration. Under the action of these comprehensive factors, the ionic conductivity of $Li_{2+x}Zr_{1-x}In_xCl_6$ increased by several orders of magnitude, and the ionic conductivity of $Li_{2.7}Zr_{0.3}In_{0.7}Cl_6$ reached up to 2.1 mS cm^{-1}. When synthesizing $Li_{2+x}Zr_{1-x}In_xCl_6$ by mechanical milling, the crystal structure changed from trigonal to monoclinic with an increase in In^{3+} content ($x \geq 0.4$) (Fig. 10d).[112] In the series of $Li_{2+x}Zr_{1-x}In_xCl_6$ prepared by this method, the ionic conductivity of $Li_{2.25}Zr_{0.75}In_{0.25}Cl_6$ was the highest (1.08 mS cm^{-1}) and decreased in the subsequent annealing process. The ionic conductivity was doubled to 0.98 mS cm^{-1} by appropriate trivalent metal ion (Fe^{3+}, V^{3+}, and Cr^{3+}) doping in hcp-Li_2ZrCl_6 (Fig. 10e).[85] On the one hand, the Fe^{3+} substitution to Zr^{4+} by trivalent metal ions relieved the coulombic repulsion between Li^+ and other metal cations, thus reducing the activation barrier for Li^+ transport. On the other hand, the trivalent metal ion substitution modulated the overall potential energy landscape and facilitated Li^+ migration. In addition, the Fe^{3+} substitution increased the number of Li^+ and

raised the concentration of effective charge carriers. The ionic conductivity of $Li_{2.25}Zr_{0.75}In_{0.25}Cl_6$ prepared by the mechanochemical method decreased sharply during annealing with an increase in crystallinity (Fig. 10f).[129]

Replacing Sc^{3+} in $Li_2Sc_{2/3}Cl_4$ with the divalent Fe^{2+} also effectively improved its ionic conductivity.[95] Due to the ionic properties, Fe^{2+} tended to replace Sc^{3+} to occupy the 16d site rather than a tetrahedral site, forming a stable octahedral framework. At the same time, the additional Li^+ occupied the 8a vacant site to maintain charge balance (Fig. 10g). In halospinel $Li_2Sc_{2/3}Cl_4$, the Li^+ diffused only through octahedral sites and 3D diffusion pathways were easily blocked by other cations located at the same site. Compared with Sc^{3+}, Fe^{2+} had a larger ionic radius and a lower oxidation number. The doped Fe^{2+} and the extra Li^+ formed new links, allowing the Oct–Oct diffusion to occur more frequently. Doped Fe^{2+} contributed to the formation of bonding networks between Li octahedra and then formed multi-diffusion channels with firm topological connectivity between the octahedra along Li diffusion pathways, thus promoting Li^+ diffusion and obtaining a high ionic conductivity of 2.72 mS cm^{-1}.

4. Synthesis methods of halide SSEs

In order to commercialize halide SSEs, the development of a stable and efficient large-scale synthesis method was key. At present, the synthesis of halide SSEs is divided into three categories: solid state reaction methods, mechanochemical synthesis, and wet chemistry synthesis (Fig. 11). The synthesis
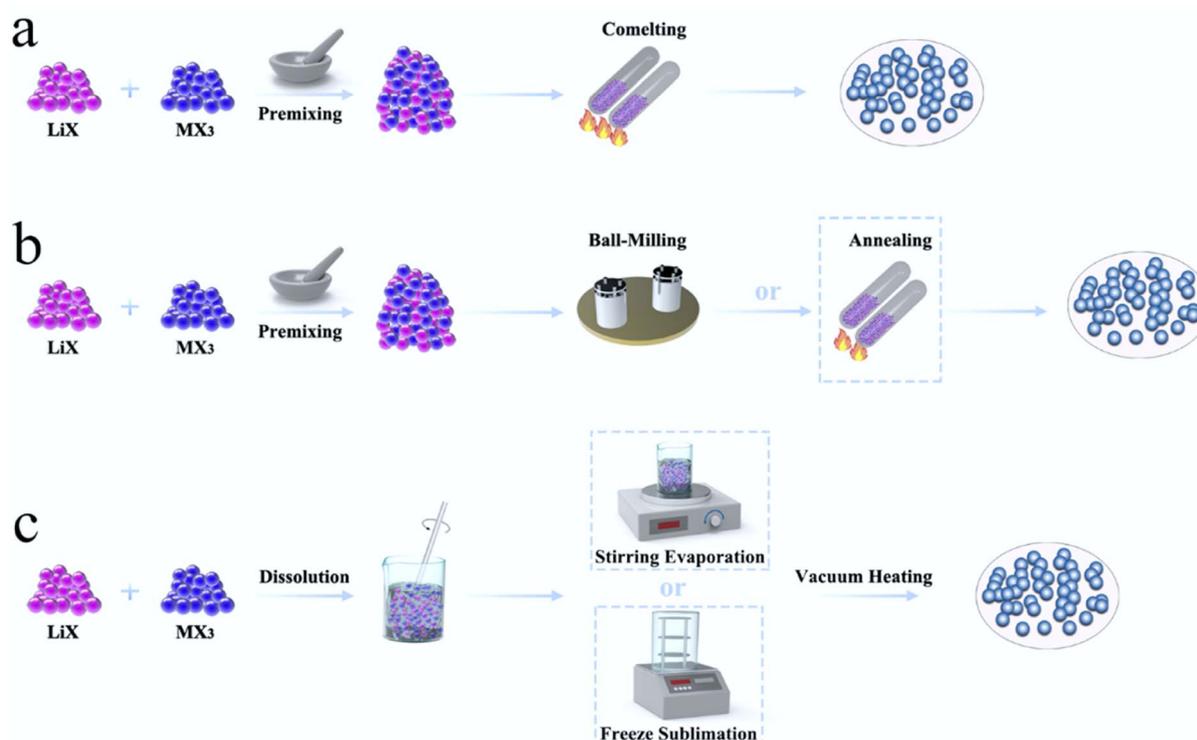

Fig. 11 Synthesis methods of halide SSEs, including (a) solid-state reaction, (b) mechanochemical synthesis and (c) wet-chemistry synthesis.

approach affected the local structure, local cationic ordering, and ion diffusion pathways of halide SSEs.[41,90,91]

4.1 Solid-state reaction

The intrinsic nature of conventional solid-state reactions required good solid–solid particle contact and enhanced the reaction kinetics by high-temperature co-melting.[130] From the viewpoint of thermodynamics, a high temperature solid-state reaction was the most likely to achieve a phase that was close to the thermodynamic equilibrium state. Due to the sensitivity of halide SSEs to moist air, the reaction was usually carried out in vacuum quartz tubes, which limited the scale-up production of electrolytes. Moreover, the solid-state reaction often needs maintaining high temperature for a long time. For example, the synthesis of $Li_3YBr_{6-x}F_x$ required heating to 950 °C for 15 h,[118] the synthesis of $Li_3YBr_xF_{6-x}$ required heating to 680 °C for 24 h,[103] and the synthesis of $Li_{4-3x}Sc_xCl_4$ required heating to 650 °C for 48 h.[45] The huge energy consumption further limited its practical applications.

4.2 Mechanochemical synthesis

Generally, the mechanochemical method allowed for the synthesis of nonequilibrium compounds. Moreover, there were large amounts of structurally disordered interfacial regions,

local distortions, and defect structures in the electrolytes by mechanochemical synthesis. The presence of these defects was advantageous for some electrolytes. For ternary trigonal chloride electrolytes, high M2/M3 site disorder played a key role in their high ionic conductivity. As shown in Fig. 12a, the ball milled Li_3YCl_6 had the lowest activation energy and the highest ionic conductivity. By the annealing treatment at different temperatures, crystallinity increased but the ionic conductivity decreased.[124] The trigonal Li_3ErCl_6, $Li_{2.6}Er_{0.6}Zr_{0.4}Cl_6$ and monoclinic Li_3ErI_6 were also consistent with this law.[39,41,83] In contrast, the ionic conductivity of Li_3YBr_6 and Li_3InCl_6 increased, with crystallinity increasing (Fig. 12b and c).[25,33,91,123] Annealing treatment could not only improve crystallinity, but also change the crystal structure of electrolyte in some cases. Li_2ZrCl_6 prepared by ball milling has a trigonal structure, which could transform into a monoclinic structure after annealing at 350 °C (Fig. 12d).[86] Although crystallinity was improved, the ionic conductivity decreased sharply. Annealing temperature was also an important parameter affecting the ion conductivity and phase structure of electrolyte (Fig. 12e).[43] After mechanochemical milling, Li_3YbCl_6 prepared at 400 °C crystallized into a trigonal structure, while the material prepared at 500 °C formed an orthorhombic structure. There was a slight difference in ionic conductivity between them. In order to obtain the as-expected ionic conductivity, it was necessary to consider the
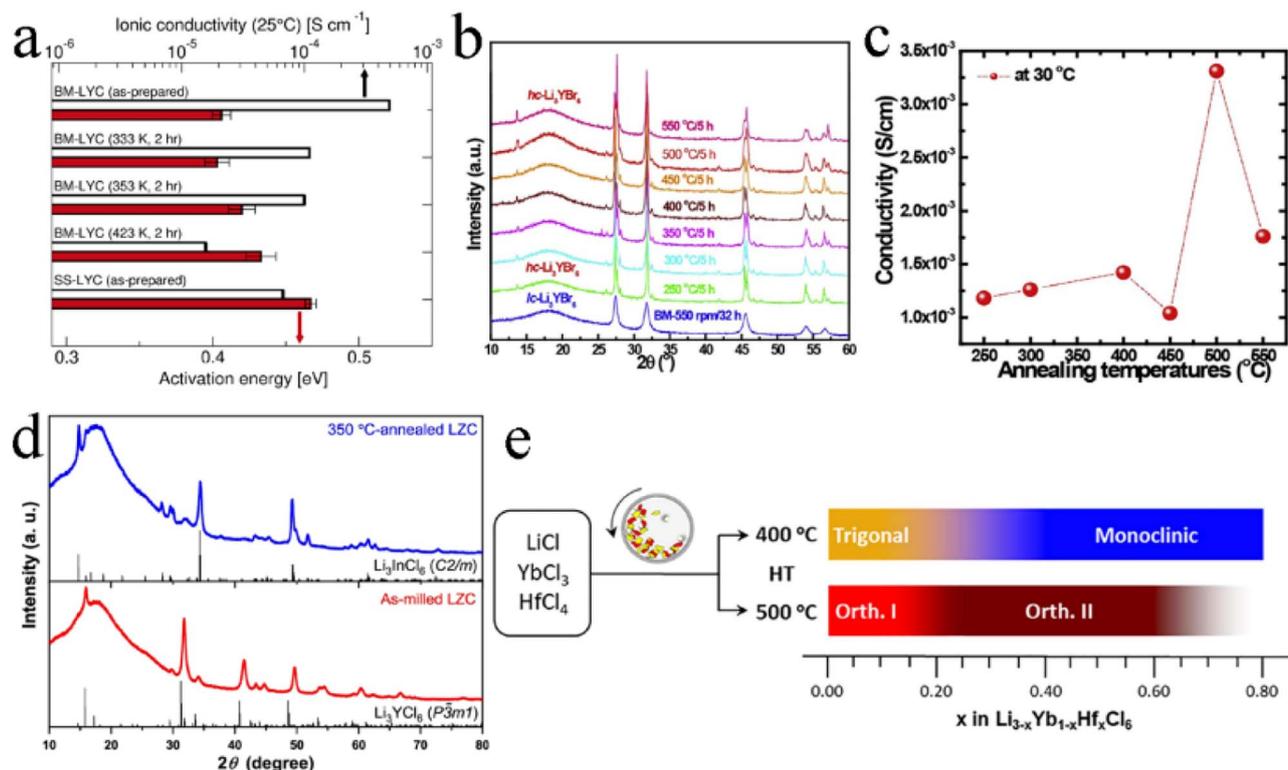
Fig. 12   (a) Room temperature ionic conductivity and activation energy for Li^+ long-range diffusion among various Li_3YCl_6 samples. Reproduced with permission.[122] Copyright 2022, American Chemical Society. (b) The XRD patterns of Li_3YBr_6 annealed at various temperatures. Reproduced with permission.[123] Copyright 2020, Elsevier Ltd. (c) Ionic conductivities of annealed Li_3YBr_6 changed with annealing temperatures. Reproduced with permission.[123] Copyright 2020, Elsevier Ltd. (d) The XRD patterns of the as-milled and annealed Li_2ZrCl_6 at 350 °C. Reproduced with permission.[86] Copyright 2020, Springer Nature. (e) Schematic illustrating the phase evolution of $Li_{3-x}Yb_{1-x}Hf_xCl_6$ at 400 or 500 °C. Reproduced with permission.[43] Copyright 2021, Elsevier B.V.

necessity of annealing and rationally select annealing temperature for the synthesis of halide SSEs by mechanochemical synthesis.

4.3 Wet chemistry synthesis

Compared with the mechanochemical and co-melting synthesis, wet chemistry synthesis could avoid long periods of high-energy ball-milling or high-temperature heating treatment and was more efficient and time-saving. Wet chemistry synthesis was the most potential route for the large-scale manufacturing of halide SSEs.

Because the dehydration/hydration process between $Li_3InCl_6 \cdot 2H_2O$ and Li_3InCl_6 was reversible and obtained high crystallinity in dehydrated Li_3InCl_6, it was feasible to use deionized water as solvent to synthesize Li_3InCl_6 on a large scale. Sun's research group was the first to synthesize Li_3InCl_6 with ionic conductivity up to 2.04 mS cm^{-1} using distilled water as the medium (Fig. 13a).[61] Through simple dissolution and vacuum heating, the high purity and crystallinity of Li_3InCl_6 could be obtained. Vacuum drying was con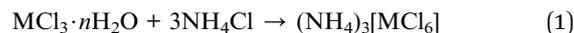ducive to the formation of small-size particles, which could completely remove trace water and avoid oxygen pollution due to a shorter diffusion length and larger surface area.[131] The particle size of Li_3InCl_6 was greatly reduced by introducing freeze drying technology into wet chemistry synthesis (Fig. 13b–d).[132] The effective removal of free water by freeze drying significantly alleviated the increase in particle size caused by particle

collision during thermal evaporation of solution. The uniform particles of electrolyte greatly reduced the porosity of ASSBs to obtain better interfacial contact and excellent cycling performance. As shown in Fig. 13e, the ASSB based on freeze-dried Li_3InCl_6 had little capacity attenuation after 150 cycles at 10C.

In addition, ethanol was also used as solvent for the synthesis of Li_3InCl_6 electrolyte.[62] The advantage of this method was that it eliminated the adverse impact of trace water on the battery performance. At the same time, this method only needed heating at 200 °C for 3 h to make the intermediate phase completely decomposed and obtain high crystallinity Li_3InCl_6 electrolyte. The raw materials (LiCl and $InCl_3$) had a very low solubility in ethanol, meaning more solvents were needed for the same amount of production. And the price of ethanol was much higher than that of deionized water, so the ethanol-mediated route showed a disadvantage in manufacturing cost.

The ammonia-assisted wet chemical synthesis was more universal, which could lift the restriction on reversible hydration/dehydration of electrolyte and extend the wet chemical route to the preparation of Li_3MX_6 (M = Y, Sc, and Er; X = Cl and Br).[63] The relevant equation is as follows:

$$MCl_3 \cdot nH_2O + 3NH_4Cl \rightarrow (NH_4)_3[MCl_6] \quad (1)$$

$$(NH_4)_3[MCl_6] + 3LiCl \rightarrow Li_3MCl_6 + 3NH_3 + 3HCl \quad (2)$$

Firstly, the NH_4^+ and MX_6 were dissolved in deionized water to form an intermediate phase. Then, the intermediate
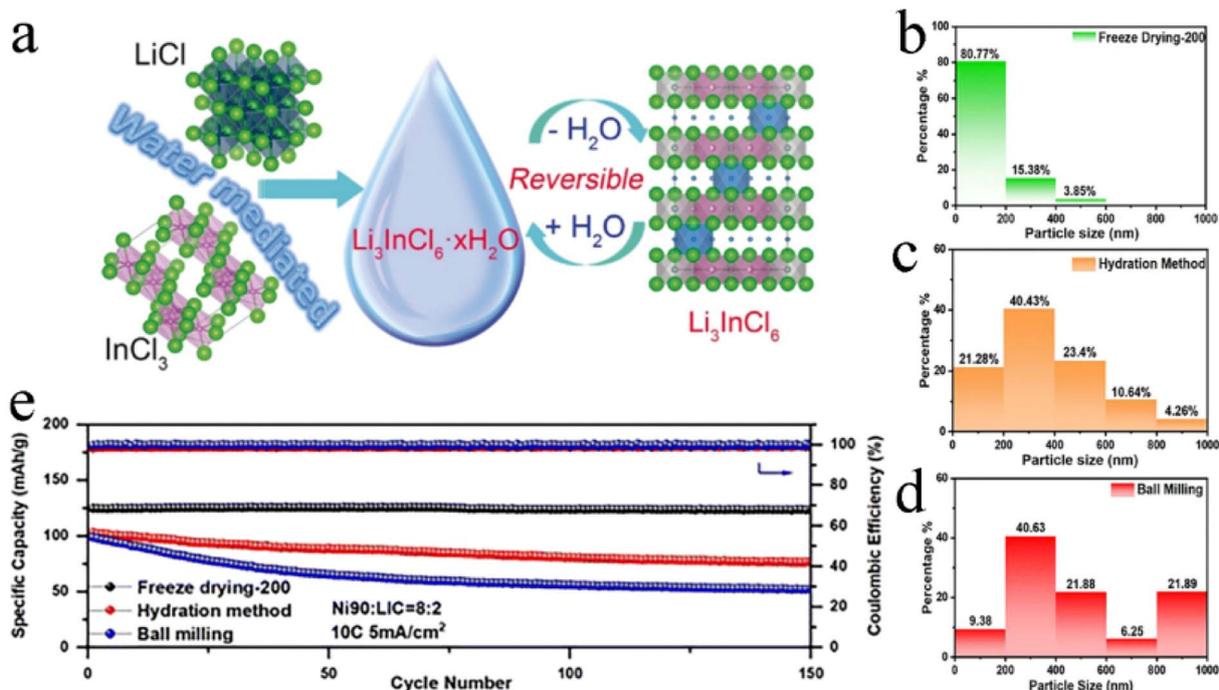
Fig. 13 (a) Illustration of a water-mediated synthesis route for Li_3InCl_6 and the reversible interconversion between hydrated $Li_3InCl_6 \cdot xH_2O$ and dehydrated Li_3InCl_6. Reproduced with permission.[61] Copyright 2019, Wiley-VCH. The histograms of the particle size distribution of Li_3InCl_6 synthesized by different methods: (b) freeze drying, (c) hydration method and (d) ball milling. Reproduced with permission.[132] Copyright 2023, The Royal Society of Chemistry. (e) Cycling performance at 10C of NCM90-Li_3InCl_6/Li_3InCl_6/Li_6PS_5Cl/Li cells with Li_3InCl_6 prepared by different methods. Reproduced with permission.[132] Copyright 2023, The Royal Society of Chemistry.

ammonium was completely decomposed after heating and the halide electrolytes with good crystallinity were obtained. The halide electrolyte synthesized by this method had nanoscale size and formed a localized microstrain in the material under the small size effect. The microstrain-induced local structural change might be favorable for Li^+ transport along the ab plane in an hcp anion framework, but not in a ccp anion sublattice.

Inspired by ammonia-assisted wet chemical synthesis, the vacuum evaporation-assisted synthesis was developed for the scale-up synthesis of Li_3HoBr_6 using the following equation:[120]

$$3Li_2CO_3 + Ho_2O_3 + 12NH_4Br \rightarrow$$
$$2Li_3HoBr_6 + 3CO_2 + 12NH_4 + 6H_2O \quad (3)$$
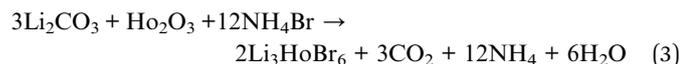
This pathway used relatively inexpensive precursors such as rare earth oxides, lithium carbonate, and ammonium halide. The ionic conductivity of synthesized Li_3HoBr_6 was equivalent to or even better than the ionic conductivity of that synthesized by the solid-state reaction method.[119]

By comparison, the wet chemistry synthesis had lower equipment requirements, cheaper raw materials, less energy consumption, and produced halide SSEs with both high ionic conductivity and electrochemical stability. In summary, wet chemistry synthesis was the most promising method for large-scale preparation of halide ASSBs.

5. Air environmental stability of halide SSEs

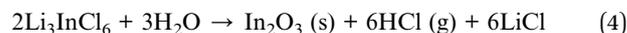Air environment stability of SSEs was always a hard-to-overcome difficulty.[133–135] It was directly related to the manufacturing cost, transportation cost, and application cost. Oxide-based SSEs had relatively good air stability, which slowly reacted with moisture and CO_2 through Li^+/H^+ exchange, formed LiOH, Li_2CO_3 and Li_2O on the surface and increased the interface resistance.[136] Sulfide-based SSEs were extremely unstable in the air, where the S^{2-} tended to bond with H^- in moist air to form toxic H_2S gas.[133] In contrast, the hydrolysis energy of ternary chloride was positive, so the reaction with water was basically stable.[137]

5.1 Degradation mechanism

Li_3InCl_6 and Li_3YCl_6 were very sensitive to moisture in the air and absorbed water quickly when exposed to air and then are completely liquefied into transparent solutions after 2 h and 8 h, respectively (Fig. 14a).[138] Li_3InCl_6 absorbed water faster than Li_3YCl_6, while Li_3YCl_6 absorbed more water than Li_3InCl_6. Their absorption rate was proportional to the contact area with moisture air. The schematic diagram of the degradation mechanism of Li_3InCl_6 is shown in Fig. 14b. Li_3InCl_6 absorbed water rapidly after being exposed to the air, to form Li_3InCl_6·$2H_2O$ crystalline hydrate in the initial stage. With the progress of the hydrolysis process, part of Li_3InCl_6 was decomposed into $InCl_3$ and LiCl, and $InCl_3$ could further hydrolyze to produce the $In(OH)_3$ intermediate phase and finally dehydrated to form In_2O_3 impurities.

In combination with types of advanced characterization methods, Li et al. revealed the degradation process of Li_3InCl_6 when exposed to humid air.[26] Li_3InCl_6 remained stable in dry air and exhibited a certain tolerance to low humidity air (3–5%), but quickly decomposed in high humidity air (30%). In general, the hydrolysis of Li_3InCl_6 proceeded according to the following two reactions:

$$2Li_3InCl_6 + 3H_2O \rightarrow In_2O_3 (s) + 6HCl (g) + 6LiCl \quad (4)$$

$$Li_3InCl_6 + xH_2O \rightarrow Li_3InCl_6·xH_2O \quad (5)$$

In moist air, hydrophilic Li_3InCl_6 first absorbed water and part of Li_3InCl_6 reacted with H_2O to form In_2O_3 as a precipitate, as well as LiCl and HCl (eqn (4)). Besides, the remaining Li_3InCl_6 absorbed H_2O to form $Li_3InCl_6·xH_2O$ hydrate (eqn (5)).

The hydration reaction of Li_3InCl_6 was a completely reversible process, and the ionic conductivity of $Li_3InCl_6·xH_2O$ could recover over 92% after removing H_2O by vacuum heating. However, the ionic conductivity of Li_3YCl_6 could only retain 0.8% after the same treatment.[25,38,61] According to the DFT, the surface adsorption energy of Li_3InCl_6 was only -0.60 eV, while the hydrolysis reaction energy barrier was high enough to inhibit the spontaneous hydrolysis reaction.[139] Fig. 14c exhibits the schematic and energy profiles of hydration and dehydration reactions of Li_3InCl_6. During hydration, Li_3InCl_6 stabilized by adsorbing H_2O on the surface. The adsorption of H_2O could reduce the surface energy below 0 J m^{-2}, making it easier to form a new surface. The newly formed surface further promoted a hydration layer on the surface of Li_3InCl_6. In the case of dehydration, the reaction was non-spontaneous and required tremendous energies to remove H_2O from the hydration phase. The monotonous reaction pathways of hydration and dehydration and their energies enabled the reversible phase evolution of Li_3InCl_6.[139] The H_2O in the $Li_3InCl_6·xH_2O$ hydrate reduced the mobility of Li by extending the required jumping distance and blocking facile migration pathways. With the removal of H_2O, the lattice shrank and the ionic conductivity was restored.[140] When the unit formula amount of H_2O was less than 0.5, the ionic conductivity of the sub-hydrate phase improved significantly, until the superionic conducting phase was formed after complete dehydration. However, the evaporation of the last trace of water contributed to the formation of stress cracks and grain boundaries (Fig. 14d).

The moisture resistance of Li_3InCl_6 came from its good recoverability after hydrolysis. By contrast, Li_2ZrCl_6 was indeed moisture resistant at relative humidity even higher than 1%.[86] Both Li_2ZrCl_6 and Li_3InCl_6 were exposed to N_2 with 5% relative humidity at the same time, and the crystal structure and ionic conductivity of Li_2ZrCl_6 remained unchanged after 24 h, whereas the ionic conductivity of Li_3InCl_6 was largely decreased by nearly an order of magnitude (Fig. 14e and f).

5.2 Strategies to improve moisture resistance

In order to improve the air stability of halide SSEs, the coating strategy is considered one of the possible solutions. Coating the surface of Li_3InCl_6 with Al_2O_3 through powder atomic layer
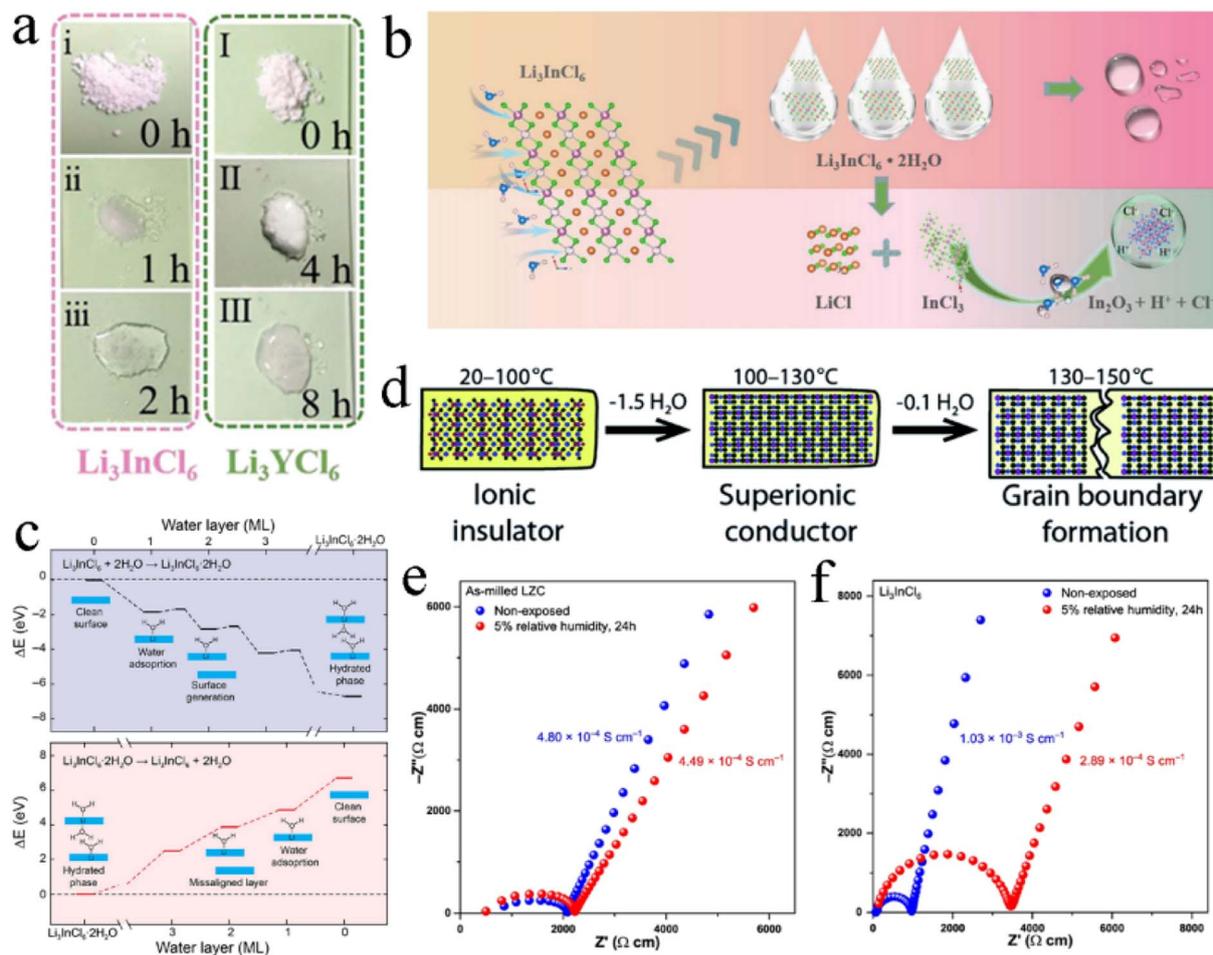
Fig. 14 (a) Images of water absorption morphology evolution of Li_3InCl_6 and Li_3YCl_6 in an air environment. Reproduced with permission.[138] Copyright 2021, Wiley-VCH. (b) Schematic diagram exhibiting the hydrolysis mechanism of Li_3InCl_6 in an air environment. Reproduced with permission.[138] Copyright 2021, Wiley-VCH. (c) Profiles of the relative energy in hydration (upper) and dehydration (below). Reproduced with permission.[139] Copyright 2021, Elsevier B.V. (d) Illustration of Li_3InCl_6 hydrate evolution during heating. Reproduced with permission.[140] Copyright 2021, The Royal Society of Chemistry. Nyquist plots of (e) as-milled Li_2ZrCl_6 and (f) Li_3InCl_6 before and after being exposed to the atmosphere with 5% relative humidity. Reproduced with permission.[86] Copyright 2021, Springer Nature.

deposition could isolate the contact with humid air, which effectively improved its moisture resistance (Fig. 15a).[138] For pristine Li_3InCl_6 with different particle sizes, the air stability time of $Li_3InCl_6@Al_2O_3$ after coating was prolonged by 4 or even 7 times. However, compared with the original Li_3InCl_6, the ionic conductivity of $Li_3InCl_6@Al_2O_3$ was slightly decreased. Also, the surface coating obviously increased manufacturing cost, which was far from a perfect solution.

The doping strategy could improve the ionic conductivity of halide SSEs and enhance their moisture resistance.[38,115] Li_3YCl_6 was unstable in air and easily changed to $YCl_3 \cdot 6H_2O$ and $LiCl \cdot H_2O$ upon contact with moisture, which was irreversible and couldn't be recovered by vacuum heating. After doping through the In^{3+}, hydration intermediates were formed when $Li_3Y_{1-x}In_xCl_6$ was exposed to moist air, rather than separated phases (Fig. 15b and c). The recovery of $Li_3Y_{1-x}In_xCl_6$ increased with an increase in In^{3+} content. When $x \geq 0.5$, the ionic conductivity of $Li_3Y_{1-x}In_xCl_6$ reheated after humidity exposure reached more than 85% that of the original material.[38] F^-

doping could greatly reduce the water absorption rate of Li_3InCl_6.[111] After exposure to a dew-point dry room (-20 ± 3 °C) for 5 h, Li_3InCl_6 retained only 22.2% of ionic conductivity, while $Li_3InCl_{5.6}F_{0.4}$ retained 62% of ionic conductivity (Fig. 15d). The increasing moisture stability might be related to the formation of robust Li–F and In–F bonds by F^- doping.[111] Inspired by the high moisture resistance of Li_2ZrCl_6, Zr^{4+} was introduced into Li_3ScCl_6 to form a robust Zr–Cl bond and improve the moisture resistance.[115] The moisture resistance of $Li_{2.5}Sc_{0.5}Zr_{0.5}Cl_6$ was obviously improved by the Zr^{4+} replacement. After being exposed to an Ar atmosphere with 5% relative humidity for 12 h, $Li_{2.5}Sc_{0.5}Zr_{0.5}Cl_6$ retained the original crystal structure and decreased its ionic conductivity by only 50%. In contrast, the ionic conductivities of Li_3ScCl_6 and Li_3InCl_6 decreased by 70% and 85%, respectively, under the same conditions (Fig. 15e). When exposed to high humidity (30% of relative humidity), $Li_{2.5}Sc_{0.5}Zr_{0.5}Cl_6$ absorbed water and further reacted with it to form a $ZrOCl_2(H_2O)_8$ phase, which could avoid the subsequent water absorption and enhanced moisture resistance.
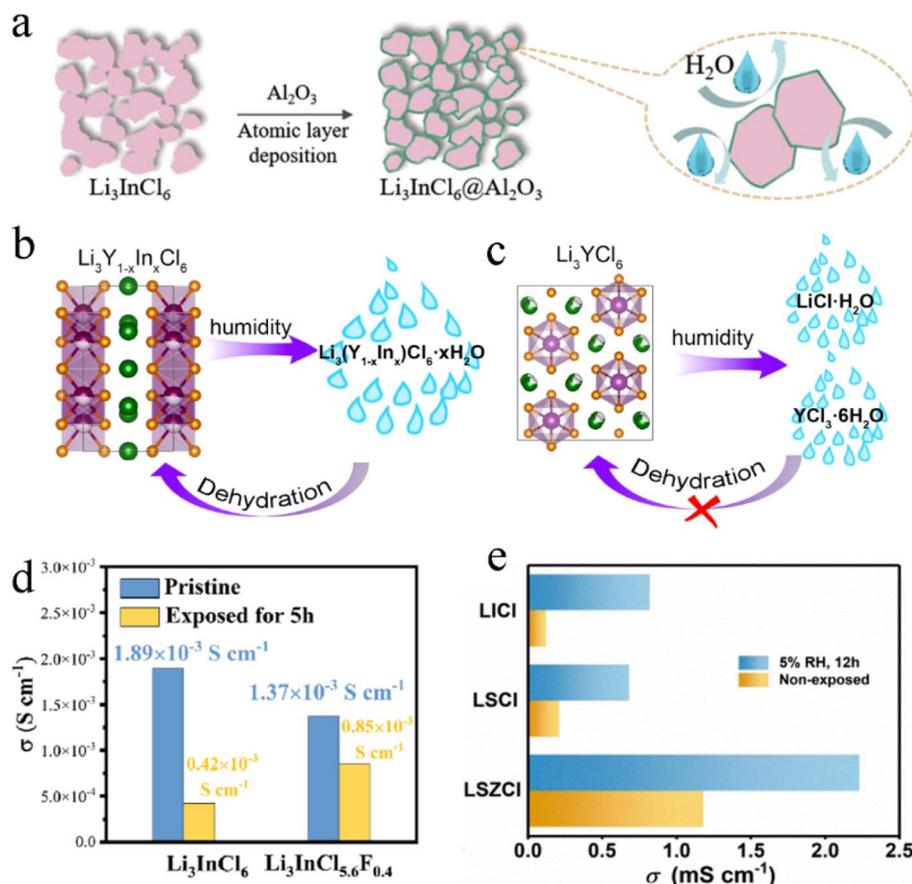
Fig. 15 (a) Schematic diagram showing that the Al_2O_3 coating enhanced Li_3InCl_6 air stability *via* powder atomic layer deposition. Reproduced with permission.[138] Copyright 2021, Wiley-VCH. Schematic illustration of the humidity stabilities of (b) $Li_3Y_{1-x}In_xCl_6$ and (c) Li_3YCl_6, respectively. Reproduced with permission.[38] Copyright 2020, American Chemical Society. (d) Ionic conductivity evolution of Li_3InCl_6 and $Li_3InCl_{5.6}F_{0.4}$ after being exposed to a dew-point dry room (-20 ± 3 °C) for 5 h. Reproduced with permission.[115] Copyright 2022, Elsevier B.V. (e) Ionic conductivity of Li_3InCl_6, Li_3ScCl_6, and $Li_{2.5}Sc_{0.5}Zr_{0.5}Cl_6$ before and after exposure to an Ar atmosphere with 5% relative humidity. Reproduced with permission.[115] Copyright 2022, Elsevier B.V.

6. Interface optimization and application challenges of halide SSEs in ASSBs

With the rapid development of halide SSEs, a series of halides with high room temperature ionic conductivity, even exceeding mS cm^{-1} have been fabricated.[33,104] The overall reaction kinetics of ASSBs were determined by ionic conductivity and also depended on interfacial resistance.[141] These halides SSEs, especially chlorides, typically had a wider electrochemical stability window than sulfides and oxides SSEs, which provided ASSBs the potential for high energy density.[96,100] However, as with other inorganic SSEs, halide electrolytes also need to overcome the interface problem with electrode materials.[20,142,143]

6.1 Interfacial stability of halide SSEs and cathodes

According to Wang *et al.*'s calculations, halide SSEs had a wide thermodynamic intrinsic electrochemical window, while sulfides and oxides couldn't match it (Fig. 16a).[27] This made

halides extremely compatible with high-voltage cathodes without the need for any protective coating.[44,46]

Almost all chloride electrolytes exhibited high oxidation potentials of $\sim$4.3 V, which could fully cover the typical working potential of cathode materials. However, chloride electrolytes and cathodes weren't stable enough against chemical decomposition, and the stability of the interface between them depended on the central metal cation and the type of cathode materials.[99,144,145] By comparing the electrochemical properties of Li_3InCl_6, $Li_2Sc_{1/3}In_{1/3}Cl_4$, and $Li_{2.5}Y_{0.5}Zr_{0.5}Cl_6$, chlorides with similar ionic conductivity, it was found that In^{3+} and Sc^{3+} central cations were beneficial for the kinetically stable interface between chloride electrolyte and the NCM85 cathode. However, some serious side reactions occurred at the interface of $Li_{2.5}Y_{0.5}Zr_{0.5}Cl_6$ and NCM85 at or above 4.3 V *vs.* Li^+/Li. The interfacial decomposition products (YOCl or ZrO_2) were conducive to the mass transfer of oxygen-containing components and promote continuous side reactions at the interface and lead to an appreciable increase of cathode impedance and a significant decay of capacity (Fig. 16b).[144] The first-principles
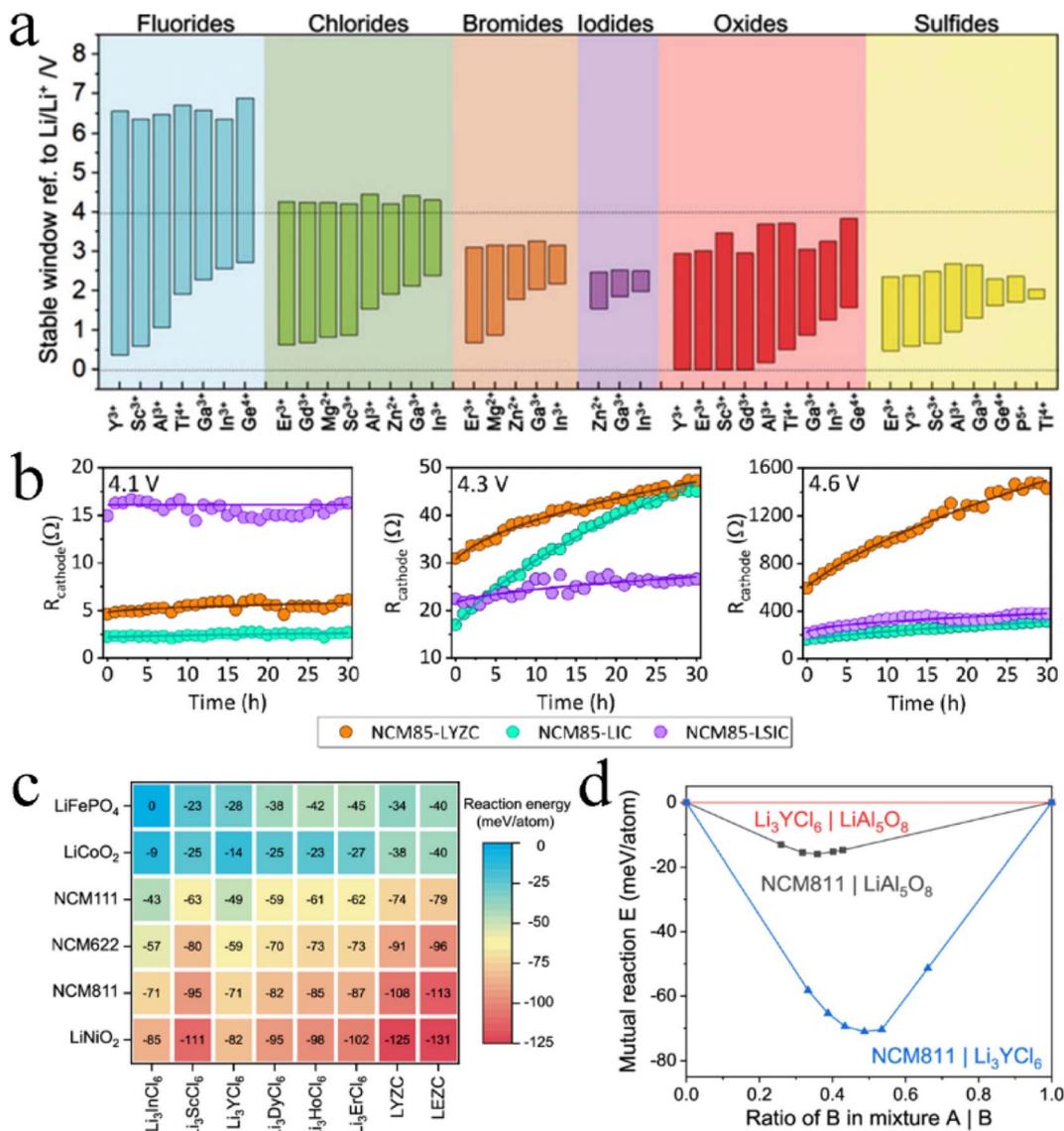
Fig. 16 (a) Comparison of thermodynamic intrinsic electrochemical windows of ternary halides, oxides, and sulfides. Reproduced with permission.[27] Copyright 2019, Wiley-VCH. (b) The cathode resistance of the charged In/InLi∥NCM85 cells during aging at 4.1–4.6 V vs. Li$^+$/Li. Reproduced with permission.[144] Copyright 2022, The Royal Society of Chemistry. (c) Heatmap of the mutual reaction energy between chloride SSEs and cathode materials. Reproduced with permission.[145] Copyright 2021, American Chemical Society. (d) Mutual reaction energy between Li$_3$YCl$_6$ and NCM811, between LiAl$_5$O$_8$ and NCM811, and between LiAl$_5$O$_8$ and Li$_3$YCl$_6$, as a function of the mixing ratio. Reproduced with permission.[145] Copyright 2021, American Chemical Society.

calculation results showed that Zr^{4+} doping significantly increased the mutual reaction energy between chloride (Li$_3$YCl$_6$ and Li$_3$ErCl$_6$) and cathode materials.[145] As shown in Fig. 16c, the mutual reaction energies between all chlorides and LiFePO$_4$ and LiCoO$_2$ (LCO) were below 50 meV per atom, indicating good chemical stability and good compatibility between chloride electrolytes and cathode materials. Similarly, LiMn$_2$O$_4$ also had low chemical reaction energy with chloride electrolytes.[99] By contrast, the Li(NiMnCo)$_{1/3}$O$_2$ (NCM111) situation wasn't so optimistic. The chemical reaction energy between NCM111 and chlorides was much higher than that of the other three anode materials, which could increase with an increase in Ni content in NCM. And therefore, NCM cathode materials weren't a good

choice for chloride electrolytes. Coating was considered a common strategy to solve SSE interface problems. From the aspects of phase stability, electrochemical stability, and chemical stability with cathode materials and chloride electrolytes, it was found that 54 Li-containing compounds were noteworthy by the high-throughput computational screening of 20 237 Li-containing compounds.[145] In Fig. 16d, the LiAl$_5$O$_8$ coating material exhibited much lower reaction energy on Li$_3$YCl$_6$ and NCM811, meaning that it could stabilize the interface between chloride electrolyte and high-voltage cathode materials. But this effect has not been confirmed by the experimental results. It was more convenient and feasible to improve the stability of the interface between chloride electrolyte and the LCO cathode by

doping F^- into dual-halogen SSE.[110] The F-doping generated F-enriched passivating interphases *in situ* on the cathode interface, which protected the electrolyte from further decomposition and was beneficial for the promising cycling stability of ASSBs. The $Li_3InCl_{4.8}F_{1.2}$-based ASSB in the voltage range of 2.6–4.47 V retained a capacity of 102 mA h g^{-1} after 70 cycles. Notably, the average coulombic efficiency was up to 99.5% during the cycling process, implying the highly reversible Li^+ de-/intercalation behavior and interfacial stability between $Li_3InCl_{4.8}F_{1.2}$ and the cathode material.

6.2 Interfacial stability of halide SSEs and anodes

Li metal is considered the "holy grail" of next-generation LIB anode materials because of its extremely high theoretical capacity of 3860 mA h g^{-1} and the lowest redox potential (-3.04 V *vs.* standard hydrogen electrode).[146,147] However, due to the low electronegativity of Li, almost all SSEs containing transition metal components were reduced upon contact with a bare Li anode.[148,149] Although a more stable interface could be obtained by replacing Li metal with a Li–In alloy, it came at the expense of capacity.

Depending on the type of central element, the reduction potential of ternary chloride electrolyte ranged from 0.7 to 2.6 V.[145] The reduction potential of chlorides with group 3 elements was slightly lower and that of group 13 elements was higher. In addition, Zr^{4+} substitution significantly increased the reduction potential of chloride electrolyte, which was an aspect to be considered when reaping the increased ionic conductivity. First-principles calculations showed that Li_3YCl_6 and Li_3ErCl_6 possessed a relatively lower decomposition energy than Li_3InCl_6 and $Li_{2.5}Y_{0.5}Zr_{0.5}Cl_6$, but they all exceeded 200 meV per atom, indicating good chemical instability with the Li metal anode. *In situ* X-ray photoelectron spectroscopy analysis of Li_3MCl_6/Li interfacial decomposition products showed that the high-valence metal cations (M^{3+}) in the chlorides were easily reduced to M^0 when they encountered Li metal, according to the following balanced chemical equation:[150]

$$Li_3MCl_6 + 3Li \rightarrow 6LiCl + M^0 \ (M^0 = In, Y)$$

The reaction product LiCl was a Li^+ conductor and M was an electron conductor, so the interphase was a mixed ionic and electronic conductor (MIEC). The MIEC interphase encouraged the continuation of thermodynamically favorable decomposition reaction and and inhibited the formation of a passivation layer.[151] Both Li^+ and electrons migrated through MIEC interphases, and the adverse side reaction continued during the Li^+ plating/stripping process until halide electrolyte or Li metal was depleted (Fig. 17a).[63,152]

Li_6PS_5Cl was the ideal protection layer to prevent direct physical contact between halide electrolyte and Li metal anode.[63,150,153] On the one hand, the Li_6PS_5Cl/halide interface had high chemical compatibility, which was conducive to the charge transfer process. On the other hand, the primary ionic conducting nature of the Li/Li_6PS_5Cl interface formed a stable self-limiting SEI layer (Fig. 17b). In addition, the good ductility

of Li_6PS_5Cl ensured that cracks couldn't form during the charge–discharge cycle. The NCM-811/Li_3YCl_6/Li_6PS_5Cl/Li full cell displayed excellent recycling ability with a capacity retention of 91% and a high coulombic efficiency of 99.7% after 100 cycles.[153] The NCM/Li_2ZrCl_6/Li_6PS_5Cl/Li–In full cell also exhibited a stable capacity of $\sim$150 mA h g^{-1} at 200 mA g^{-1} after 200 cycles.[86] The Li/Li_6PS_5Cl–Li_2ZrCl_6/LCO cell showed good cycling stability over 70 cycles at a 0.1C rate, with a capacity retention of 80.5% and coulombic efficiency of up to 100%. By contrast, the Li/Li_2ZrCl_6/LCO cell lost more than 70% of its capacity after only 3 cycles, due to severe side reactions between Li_2ZrCl_6 and the Li metal anode.[154] However, the other experimental results showed that Li_6PS_5Cl and Li_3InCl_6 were chemically incompatible.[155–157] The parasitic reaction occurred when these two came into direct contact and formed the indium sulfide-like compound in the interfacial region, which resulted in interfacial deterioration and an increase in interfacial resistance. These weren't conducive to the cycle performance of ASSBs. Moreover, Li_6PS_5Cl possessed intrinsic chemical incompatibility with high voltage cathode materials.[158,159] Li_6PS_5Cl was oxidatively decomposed in the reaction voltage range of NCM811 to produce Li_2S, P_2S_5, Li_2S_n, and other phosphorus species. The molar volume of these decomposition products was smaller than that of original Li_6PS_5Cl, forming large numbers of voids between Li_6PS_5Cl and the NCM cathode material. This was greatly detrimental to the cycle stability of ASSBs.

Due to the limitations of Li_6PS_5Cl, it was necessary to screen out the coating materials that were compatible with halide electrolytes and cathode materials to improve the stability of the interface.[145] According to calculations, the oxidation potential of binary halides (LiF, LiCl, LiBr, and LiI) and oxides (Li_2O) was higher than the reduction potential of Li_3InCl_6, which could be used as efficient coating materials. And Li_2S, Li_2Se, and Li_3P with a narrow electrochemical stability window were only suitable for Li_3MCl_6 with group 3 elements. As shown in Fig. 17c, the reaction energy between Li_3N and chloride exceeded 100 meV per atom, with the risk of a chemical decomposition reaction. However, it was proved that β-Li_3N could be used as a coating material to improve the interfacial stability of Li_2ZrCl_6 and the Li metal anode.[160] β-LiN_3 was an excellent ionic conductor and electrical insulator and was fully compatible with Li metal. β-Li_3N could prevent direct physical contact between the halide SSE and Li metal to avoid interface side reactions. Furthermore, the high ionic conductivity of β-Li_3N didn't hinder the rapid ion migration of Li^+ and was conducive to the plating/stripping homogenization of Li metal. The β-Li_3N layer dramatically reduced the interfacial impedance between the halide SSE and Li anode and effectively heightened the interfacial stability. It was reported that the Li_6PS_5Cl and Li_3N mixture effectively inhibited the growth of Li dendrites, thus improving the rate capability and cycle stability of ASSBs.[159] Amorphous $LiNbO_3$ reduced the oxidation decomposition of Li_3YCl_6 at a high voltage of $\sim$4.5 V in the cycle process, so as to ensure the chemical and electrochemical compatibility between electrolyte and electrode materials.[158]

In addition, F^- doping could also greatly improve the cycle stability of ASSBs.[110,111,118] Compared with Cl^- and Br^-, the F^- in
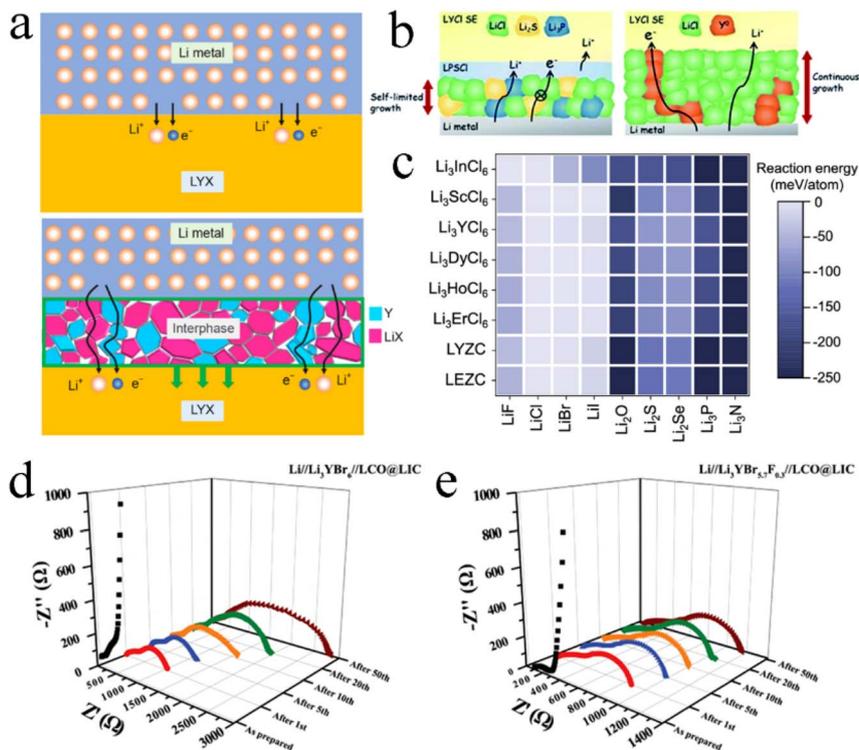
Fig. 17 (a) Schematic illustration of the reaction of LYX electrolyte and the Li anode. Once LYX electrolyte was in contact with Li metal, it was reduced to form a Y and LiX interphase that could conduct both Li$^+$ and electrons, allowing the adverse side reaction to continue. Reproduced with permission.[152] Copyright 2021, Science China Press and Springer. (b) Schematic illustration showing the mechanism of LPSCl action on the interface stability. Reproduced with permission.[153] Copyright 2021, The Royal Society of Chemistry. (c) Heatmap of the reaction energy between binary coating materials and lithium chloride electrolyte. Reproduced with permission.[145] Copyright 2021, American Chemical Society. The EIS evolution at different cycles of (d) Li//Li$_3$YBr$_6$//LCO@LIC and (e) Li//Li$_3$YBr$_{5.7}$F$_{0.3}$//LCO@LIC cells. Reproduced with permission.[116] Copyright 2021, Wiley-VCH.

halide SSEs had shorter and stronger bonds with Li, thus causing local distortion in the local Li coordination environment, increasing the barrier for Li$^+$ migration and slightly reducing the ionic conductivity. Although the F$^-$ doped Li$_3$-YBr$_{5.7}$F$_{0.3}$ was still unstable to Li metal, a consecutive and homogeneous fluoride (LiF and YF$_x$) layer was formed at the interface during the charging/discharging process, which could effectively inhibit interface side reactions and guarantee long cycling durability. The interface resistance between Li$_3$YBr$_{5.7}$F$_{0.3}$ and the Li metal anode was relatively stable and was increased by only 300 Ω after 50 cycles (Fig. 17e). Using Li$_3$YBr$_{5.7}$F$_{0.3}$ as electrolyte, the Li plating/stripping maintained over 1000 h at 0.75 mA cm^{-2}, and the Li//Li$_3$YBr$_{5.7}$F$_{0.3}$//LCO@LIC cell could still retain 60% of discharge capacity and 99% of Coulomb efficiency after 70 cycles. In contrast, the side reactions between undoped Li$_3$YBr$_6$ and the Li metal interface continue to occur, contributing to the non-homogeneous deposition of Li$^+$, increased interface polarization, interface structure decomposition, and contact failure. The interface resistance between Li$_3$YBr$_6$ and the Li metal anode increased significantly and reached about 3000 Ω in the 50th cycle (Fig. 17d). The plating/stripping potential of the cell with Li$_3$YBr$_6$ increased gradually after 50 h and short-circuit failure occurred after 500 h. The ASSB assembled based on Li$_3$YBr$_6$ could only retain 12% of its

discharge capacity after 70 cycles. By introducing Zr^{4+} into Li$_3$-InCl$_6$, the system formation energy was reduced and the stability between Li$_{3-x}$In$_{1-x}$Zr$_x$Cl$_6$ and the Li metal anode was improved. No chemical reaction occurred after the direct contact between Li$_{3-x}$In$_{1-x}$Zr$_x$Cl$_6$ and Li metal for 24 h, while the side reaction occurred and formed a visible black spot on the Li metal sheet surface when Li$_3$InCl$_6$ came into contact with Li metal.[108]

6.3 Halide SSEs for high voltage ASSBs

Halide SSEs could combine the advantages of oxides and sulfides and exhibited good mechanical formability, considerable ionic conductivity, and excellent electrochemical oxidation stability and were outstanding candidates for next generation LIBs. After solving the interface problem with the Li metal anode, halide-based ASSBs always showed excellent electrochemical performance.[156,161,162] The satisfactory capacity and rate performance of ASSLBs with halide SSEs and high voltage Li-enriched oxide cathode materials are summarized in Table 2.

Zr was more abundant in the Earth's crust than other rare earth elements, which gave Li$_2$ZrCl$_6$-based ASSBs an advantage in terms of raw material cost (Fig. 18a). In addition, Li$_2$ZrCl$_6$ had excellent moisture resistance and further reduced storage cost and manufacturing cost. Therefore, Li$_2$ZrCl$_6$ exhibited

Table 2 Summary of electrochemical performances of halide-based ASSBs[a]

Cathode	Solid electrolyte	Separator	Anode	Voltage range vs. Li$^+$/Li [V]	Cell performance [mA h g^{-1}] First cycle CE [%]/capacity	Capacity/current density/cycle	Ref.
LCO@Li$_3$YCl$_6$	Li$_3$YCl$_6$	—	Li–In	2.5–4.2	94.8/119	111/0.1C/100	31
NCM811@Li$_3$YCl$_6$@C	Li$_3$YCl$_6$	Li$_6$PS$_5$Cl	Li	2.9–4.3	87/181	164.7/0.1 mA cm^{-2}/100	153
LiNi$_{0.88}$Co$_{0.11}$Al$_{0.01}$O$_2$/Li$_3$YCl$_6$@SC	Li$_3$YCl$_6$	—	Li–In	3.0–4.3	89.6/199	192.6/0.1/200	28
LCO@Li$_3$InCl$_6$	Li$_3$InCl$_6$	Li$_{10}$GeP$_2$S$_{12}$	Li–In	3.1–4.2	92.7/132	90.3/0.5C/200	163
NCM811@Li$_3$InCl$_6$@C	Li$_3$InCl$_6$	Li$_{10}$GeP$_2$S$_{12}$	Li–In	1.9–3.8	80.44/174.8	165.7/0.1C/200	62
NCM811@Li$_3$InCl$_6$	Li$_3$InCl$_6$	Li$_{10}$GeP$_2$S$_{12}$	Li–In	1.9–3.8	84.2/154	150/0.13 mA cm^{-2}/70	61
LCO@Li$_3$InCl$_6$	Li$_3$InCl$_6$	Li$_6$PS$_5$Cl	Li	2.5–4.2	—/125	124/10C/150	132
LCO@Li$_3$InCl$_6$	Li$_3$InCl$_6$	Li$_{10}$GeP$_2$S$_{12}$	Li	2.5–4.2	92/127	95/0.1/100	25
LCO@Li$_3$InCl$_{4.8}$F$_{1.2}$	Li$_3$InCl$_{4.8}$F$_{1.2}$/Li$_3$InCl$_6$	Li$_6$PS$_5$Cl	In	2.6–4.47	92/160.6	102/0.125 mA cm^{-2}/70	110
LCO@Li$_{2.7}$In$_{0.7}$Hf$_{0.3}$Cl$_6$	Li$_{2.7}$In$_{0.7}$Hf$_{0.3}$Cl$_6$	Li$_6$PS$_5$Cl	Li–In	3.0–4.2	92.2/104.4	76.3/0.1C/50	88
LCO@Li$_2$ZrCl$_6$	Li$_2$ZrCl$_6$	Li$_6$PS$_5$Cl	Li–In	1.9–3.6	97.9/137	114/0.5C/100	86
NCM811@Li$_2$ZrCl$_6$	Li$_2$ZrCl$_6$	Li$_6$PS$_5$Cl	Li–In	2.2–3.8	90.3/181	181/0.1C/200	86
NCM622@Li$_2$ZrCl$_6$	Li$_2$ZrCl$_6$	Li$_6$PS$_5$Cl	Li	3.0–4.3	96.1/158.8	138.3/0.3C/70	154
LCO@Li$_2$ZrCl$_6$	Li$_2$ZrCl$_6$	—	Li–In	3.0–4.3	91.4/156	142.1/0.1C/100	85
LiNi$_{0.88}$Co$_{0.11}$Al$_{0.01}$O$_2$/Li$_{2.25}$Zr$_{0.75}$Fe$_{0.25}$Cl$_6$/SC	Li$_{2.25}$Zr$_{0.75}$Fe$_{0.25}$Cl$_6$	—	Li–In	3.0–4.3	85.8/206	188.1/0.5C/100	85
LiNi$_{0.6}$Co$_{0.2}$Mn$_{0.2}$O$_2$@Li$_{2.25}$Zr$_{0.75}$Fe$_{0.25}$	Li$_{2.25}$Zr$_{0.75}$Fe$_{0.25}$Cl$_6$	Li$_{5.5}$PS$_{4.5}$Cl$_{1.5}$	In–Li	3.0–4.3	86.99/153.1	105.5/0.2C/90	129
NCM88@Li$_{2.5}$Zr$_{0.5}$In$_{0.5}$Cl$_6$@SC	Li$_{2.5}$Zr$_{0.5}$In$_{0.5}$Cl$_6$	Li$_6$PS$_5$Cl	Li–In	3.0–4.3	87.2/202	174.5/0.5C/100	105
LCO@Li$_3$ScCl$_6$	Li$_3$ScCl$_6$	—	In	2.5–4.2	90.3/126	104.5/0.1/160	24
NCM@Li$_3$ScCl$_6$	Li$_3$ScCl$_6$	Li$_6$PS$_5$Cl	Li	2.8–4.4	85.6/166.9	85.9/0.2C/100	63
NMC622@Li$_2$Sc$_{2/3}$Cl$_4$	Li$_2$Sc$_{2/3}$Cl$_4$	Li$_{6.7}$Si$_{0.7}$Sb$_{0.3}$S$_5$I	Li–In	2.8–4.5	93.9/180	170/0.1C/110	45
LCO@Li$_2$Sc$_{2/3}$Cl$_4$	Li$_2$Sc$_{2/3}$Cl$_4$	Li$_{6.7}$Si$_{0.7}$Sb$_{0.3}$S$_5$I	Li–In	3.0–4.3	93.7/135	120/1C/70	45
NCM622@Li$_2$In$_{1/3}$Sc$_{1/3}$Cl$_4$	Li$_2$In$_{1/3}$Sc$_{1/3}$Cl$_4$	Li$_{6.7}$Si$_{0.7}$Sb$_{0.3}$S$_5$I	In/In–Li	2.8–4.6	—/194	180/0.2C/320	46
NCM85@Li$_2$In$_{1/3}$Sc$_{1/3}$Cl$_4$	Li$_2$In$_{1/3}$Sc$_{1/3}$Cl$_4$	Li$_{6.7}$Si$_{0.7}$Sb$_{0.3}$S$_5$I	In/In–Li	2.8–4.3	—/200	180/0.2/600	46
NCM85@Li$_2$In$_{1/3}$Sc$_{1/3}$Cl$_4$	Li$_2$In$_{1/3}$Sc$_{1/3}$Cl$_4$	Li$_{6.7}$Si$_{0.7}$Sb$_{0.3}$S$_5$I	In/In–Li	2.8–4.3	—/90	72/3C/3000	46
NCM811@Li$_{2.5}$Sc$_{0.5}$Zr$_{0.5}$Cl$_6$	Li$_{2.5}$Sc$_{0.5}$Zr$_{0.5}$Cl$_6$	Li$_6$PS$_5$Cl	Li–In	2.8–4.3	89.6/203.6	174.5/0.2C/200	115
LCO@Li$_{2.6}$Er$_{0.6}$Zr$_{0.4}$Cl$_6$@VGCF	Li$_{2.6}$Er$_{0.6}$Zr$_{0.4}$Cl$_6$	Li$_6$PS$_5$Cl	Li–In	3.0–4.2	97.4/140	106.4/0.1C/500	39
LCO@Li$_{2.633}$Er$_{0.633}$Zr$_{0.367}$Cl$_6$	Li$_{2.633}$Er$_{0.633}$Zr$_{0.367}$Cl$_6$	Li$_3$PS$_4$	Li$_{11}$Sn$_6$	3.0–4.3	96.4/110	80/0.5C/200	44
NCA88@Li$_{2.6}$Yb$_{0.6}$Hf$_{0.4}$Cl$_6$@SC	Li$_{2.6}$Yb$_{0.6}$Hf$_{0.4}$Cl$_6$	Li$_6$PS$_5$Cl$_{0.5}$Br$_{0.5}$	Li–In	3.0–4.3	84.8/188	157.2/0.5C/1000	43
LCO@Li$_{2.556}$Yb$_{0.492}$Zr$_{0.492}$Cl$_6$	Li$_{2.556}$Yb$_{0.492}$Zr$_{0.492}$Cl$_6$	Li$_{10}$GeP$_2$S$_{12}$	In–Li	2.5–4.5	93.3/193.9	159.2/0.3C/50	100
LCO@Li$_3$YBr$_6$	Li$_3$YBr$_6$	—	Li–In	2.5–4.2	94.2/120	117/0.1C/100	33
NMC811@Li$_3$YBr$_6$	Li$_3$YBr$_6$	Li$_{5.7}$PS$_{4.7}$Cl$_{1.3}$	In	2.5–4.4	—/180.2	67.8/0.127 mA cm^{-2}/90	121
LCO@Li$_3$InCl$_6$@Li$_3$YBr$_{5.7}$F$_{0.3}$	Li$_3$YBr$_{5.7}$F$_{0.3}$	—	Li	2.5–4.2	89/126.7	85.1/0.1 mA cm^{-2}/70	118
NCM523@Li$_{0.388}$Ta$_{0.238}$La$_{0.475}$Cl$_3$@VGCF	Li$_{0.388}$Ta$_{0.238}$La$_{0.475}$Cl$_3$	—	Li	2.2–4.35	84.96/163	138.5/0.44C/100	17
NCM91@LiTaCl$_6$	LiTaCl$_6$	Li$_{5.4}$PS$_{4.4}$Cl$_{1.6}$	Li–In	2.5–4.8	91.17/232.39	207.6/0.3C/200	117
LCO@ZrO$_2$–2Li$_2$ZrCl$_6$@C65	ZrO$_2$–2Li$_2$ZrCl$_6$	Li$_6$PS$_5$Cl	Li–In	3.0–4.3	95.4/156	134.1/82 mA g^{-1}/100	114

[a] SC: super C; VGCF: vapour-grown carbon fibre.

broad application prospects. Li$_2$ZrCl$_6$ with the as-expected ionic conductivity could be prepared by ball milling, and then Li$_2$ZrCl$_6$-based ASSBs with excellent performance could be fabricated by the facile cold pressing method.[86] The LCO/Li$_2$ZrCl$_6$/Li$_6$PS$_5$Cl/Li–In cell exhibited an initial discharge capacity of 137 mA h g^{-1} and a Coulomb efficiency of 97.9% at 0.1C between 1.9 and 3.6 V. After 100 cycles at 0.5C, the capacity was 114 mA h g^{-1} and the Coulomb efficiency reached 99.9%. By replacing the cathode material with NMC811, the performance of ASSBs could be further improved. The NMC811/Li$_2$ZrCl$_6$/Li$_6$PS$_5$Cl/Li–In cell could deliver an initial discharge capacity of 181 mA h g^{-1} and a Coulomb efficiency of 90.3% at 0.1C between 2.2 and 3.8 V. After 200 cycles at 1C, the capacity was

149 mA h g^{-1} and the Coulomb efficiency was 99.9%. After the Fe doping, the rate performance of Li$_2$ZrCl$_6$ was further improved.[85]

Li$_3$InCl$_6$ could be synthesized through a H$_2$O-mediated synthesis route, which reduced the requirement for a manufacturing facility and had the potential for scale-up production. Li$_3$InCl$_6$ synthesized by mechanochemistry had better cycling stability and reversible capacity than Li$_{10}$GeP$_2$S$_{12}$ (Fig. 18b). The LCO/Li$_3$InCl$_6$/Li–In cell still had a specific capacity of 95 mA h g^{-1} after 100 cycles at 0.1C.[25] Li$_3$InCl$_6$ synthesized by the wet-chemistry method also showed a stable cycling performance. The LCO/Li$_3$InCl$_6$/Li$_{10}$GeP$_2$S$_{12}$/In cell exhibited an initial reversible specific capacity of 154 mA h g^{-1}
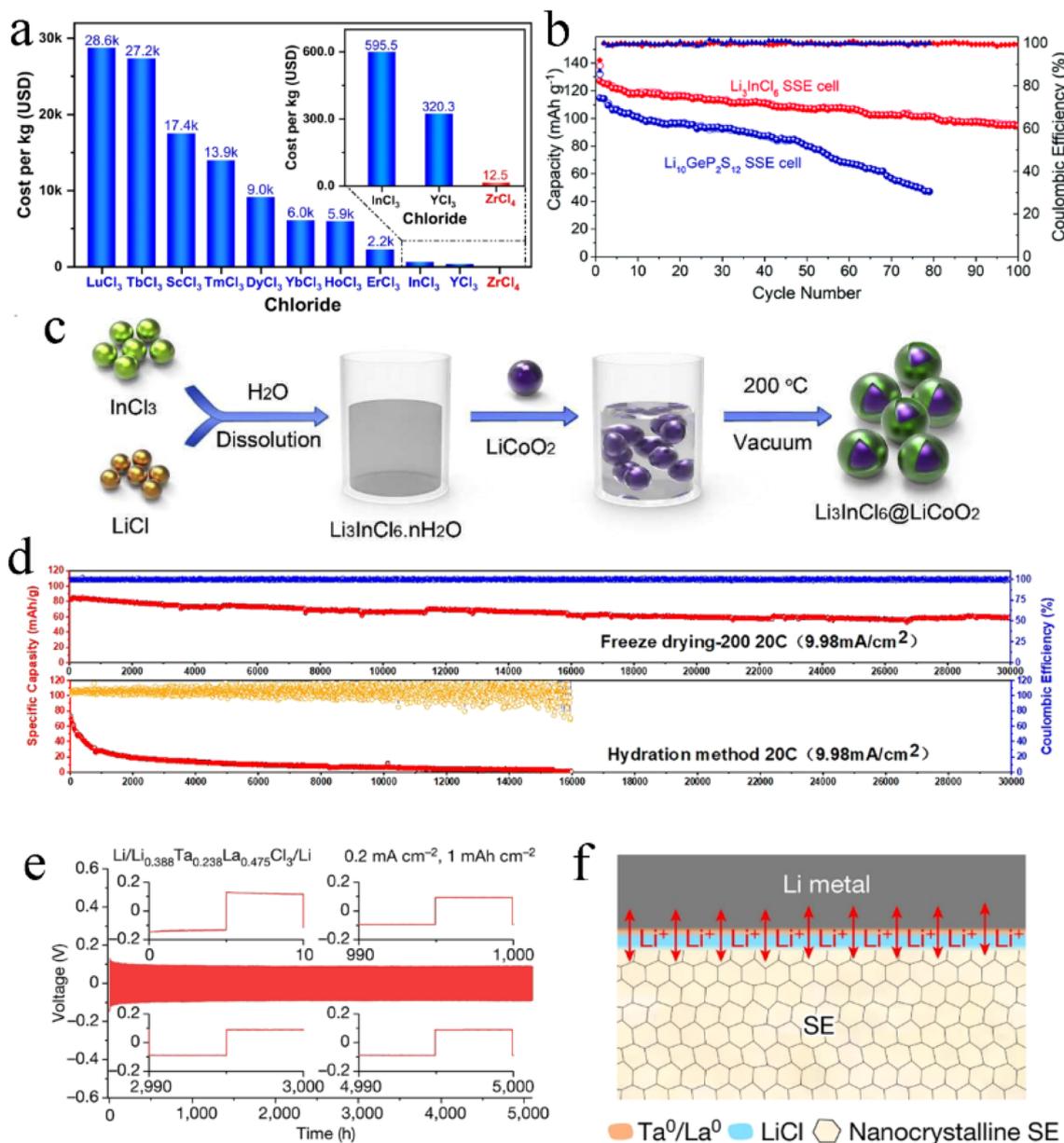
Fig. 18 (a) The price per unit of raw materials required for the synthesis of different chloride SSEs. Reproduced with permission.[86] Copyright 2021, Springer Nature. (b) The cycling performance and coulombic efficiency of LiCoO$_2$@Li$_3$InCl$_6$/Li$_3$InCl$_6$/In and LiCoO$_2$@Li$_{10}$GeP$_2$S$_{12}$/Li$_{10}$-GeP$_2$S$_{12}$/In cells at 0.1C. Reproduced with permission.[25] Copyright 2019, The Royal Society of Chemistry. (c) Illustration of the *in situ* synthesis of Li$_3$InCl$_6$ on the LCO surface. Reproduced with permission.[163] Copyright 2020, Elsevier Ltd. (d) Cycling performance of the LCO/Li$_3$InCl$_6$/Li$_6$PS$_5$Cl/ Li cell at 20C. Reproduced with permission.[132] Copyright 2023, The Royal Society of Chemistry. (e) Voltage profile of the Li/Li$_{0.388}$Ta$_{0.238}$-La$_{0.475}$Cl$_3$/Li symmetric cell cycled at a current density of 0.2 mA cm^{-2} at 30 °C. Reproduced with permission.[17] Copyright 2023, Springer Nature. (f) Schematic of the gradient structural interphase layer generated at the Li/Li$_{0.388}$Ta$_{0.238}$La$_{0.475}$Cl$_3$ interface. Reproduced with permission.[17] Copyright 2023, Springer Nature.

and retained up to ~150 mA h g^{-1} after 70 cycles.[61] Li$_3$InCl$_6$ could be grown *in situ* on the surface of the LCO cathode for intimate solid–solid contact and ultra-small interfacial resistance (Fig. 18c).[163] The LCO@Li$_3$InCl$_6$ composite cathode delivered an initial discharge capacity of 131.7 mA h g^{-1} and a coulombic efficiency of 92.7% at 0.1C. After 200 cycles, the capacity retention rate was 68.6%. By refining the Li$_3$InCl$_6$ particles, the performance of the ASSB was further improved.[132] Small electrolyte particles were conducive to interfacial contact

and ion transportation, which were the basis of achieving excellent rate performance and cycle performance. Most of the Li$_3$InCl$_6$ particles prepared by freeze-drying technology were less than 200 nm in diameter. The LCO/Li$_3$InCl$_6$/Li$_6$PS$_5$Cl/Li cell reached an initial capacity of 201 mA h g^{-1} at 0.5C or even 125 mA h g^{-1} at a high rate of 10C and then released a capacity of 124 mA h g^{-1} after 150 cycles at 10C. Even up to 49C, the Li$_3$InCl$_6$-based ASSB could still be charged and discharged normally, with a capacity of 17 mA h g^{-1}. At 20C, the LCO/

$Li_3InCl_6/Li_6PS_5Cl/Li$ cell had an ultra-long cycle life, and the capacity retention rate reached 70 after 30 000 cycles (Fig. 18d). The ASSB fabricated with the large-particle Li_3InCl_6 failed completely after 16, 000 cycles.

Yin *et al.* reported a novel chloride electrolyte $Li_{0.388}Ta_{0.238}La_{0.475}Cl_3$, with a room temperature ionic conductivity of 3.02 mS cm^{-1} and stability with a Li metal electrode.[17] In the Li/$Li_{0.388}Ta_{0.238}La_{0.475}Cl_3$/Li symmetric cell, the interphase impedance only increased slightly during the first 20 h and then stabilized at 5000 h (Fig. 18e), which was better than that of the inorganic SSEs previously reported. This was due to the formation of a dense gradient interface passivation layer during the Li stripping/plating (Fig. 18f). The passivation layer isolated the direct contact between electrolyte and Li metal, relieved the interfacial strain and inhibited the growth of Li dendrites. Thus, $Li_{0.388}Ta_{0.238}La_{0.475}Cl_3$-based ASSBs used bare Li metal as an anode without the need for an extra buffer layer. The Li/$Li_{0.388}Ta_{0.238}La_{0.475}Cl_3$/NCM523 full cell delivered a specific capacity of 163 mA h g^{-1} at a 0.44 C rate and an initial coulombic efficiency of 84.96%. After 100 cycles in the cut-off voltage range of 2.2–4.35 V, the capacity retention was 81.6%.

Halide SSEs could also be used in other ASSBs. The $Se@Li_3HoCl_6@C/Li_3HoCl_6$/Li cell exhibited a reversible capacity of 402 mA h g^{-1} at 0.1C after 750 cycles.[89] The Li/$Li_7P_3S_{11}/Li_3HoBr_6$/S cell could maintain high coulombic efficiency (close to 100%) at 0.2C after 400 cycles.[119] Li_3InCl_6 could be used as an interlayer to improve the stability of the $Li_{10}SnP_2S_{12}$-based ASSB's cathode interface.[164] Li_3InCl_6 could also be used to modify the interface for high-performance solid-state Li–O$_2$ batteries.[165] Li_3TiCl_6 could be used as a positive electrode active material for $Li_3TiCl_6/Li_2ZrCl_6/Li_6PS_5Cl/Li$–In cells with an initial capacity of 92.5 mA h g^{-1} at 0.1C.[92] After 2500 cycles, the capacity retention was 62.3% and the final coulombic efficiency was as high as 99.7%. The halide–sulfide hybrid SSEs formed by the combination of Li_3YCl_6 and Li_6PS_5Cl showed excellent electrochemical performance in terms of discharge capacity, rate capability and cycling performance.[166]

7. Conclusion and outlook

In summary, this review presented the cognition and understanding of halide SSEs and their applications in ASSBs. Firstly, the screening principle of halide SSE composition was proposed. With the assistance of computational simulation, Cl$^-$ was considered to be the most suitable halogen anion because of chloride's ability to well balance ionic conductivity and the electrochemical stability window. Group 3 elements (Sc, Y, and lanthanides) were the most promising metal cations because they matched the electronegativity of halogen anions. Secondly, the theory of structural design of halide electrolytes with high ionic conductivity and the mechanism of Li ion migration were described. Compared with trigonal and orthorhombic structures, the monoclinic structure-based electrolyte had a 3D diffusion pathway with a low energy barrier and obtained higher ionic conductivity. Additionally, strategies for halide SSEs were discussed, including dual-halogen, isovalent cation substitution, and aliovalent cation substitution. Reasonable

substitution could improve the ionic conductivity of halide SSEs, broaden the electrochemical stability window, and enhance moisture resistance. Furthermore, the mechanism of moisture resistance and synthesis of halide electrolytes were analyzed. Wet chemical synthesis was the most potential method, which had the advantages of convenience and high efficiency and was beneficial for scale-up preparation of halide SSEs. Finally, the applications of halide SSEs in ASSBs were outlined. Li_2ZrCl_6 had more advantages in terms of cost, while Li_3InCl_6 was outstanding in terms of electrochemical performance. A Li_3InCl_6-based ASSB could cycle normally up to 30 000 times at a high rate of 20C.

Although halide SSEs ushered in their second spring since 2018 and made breakthrough progress in recent years, to achieve commercial applications as soon as possible, there are still urgent issues to be solved in the following aspects.

(1) The upper limit of ionic conductivity for halide SSEs is still an open question. Although the formation of dual-halogen SSEs by haloanion substitution makes the ionic conductivity of $Li_3Y(Br_3Cl_3)$ reach up to 7.2 mS cm^{-1}, enough to be comparable to that of sulfide SSEs known for their high ionic conductivity, there is still a significant gap from theoretical prediction. Some strategies should be used to try to narrow this gap, such as defect design and grain boundary enhancement.

(2) At present, halide SSEs with high ionic conductivity mainly rely on rare earth metals as central elements, resulting in high raw material cost. Li_2ZrCl_6 can greatly reduce the manufacturing cost, but its ionic conductivity is only 0.81 mS cm^{-1}. Through partial substitution of Sc, the ionic conductivity of $Li_{2.5}Sc_{0.5}Zr_{0.5}Cl_6$ reaches 2.23 mS cm^{-1}, which is still not outstanding. Other substitution strategies are needed to further improve the ionic conductivity of Li_2ZrCl_6 under the premise of controlling the cost of raw materials.

(3) Wet chemistry synthesis is the most convenient and efficient preparation method, which can realize the large-scale manufacturing of halide SSEs. The H_2O-mediated synthesis route is only applicable to Li_3InCl_6. Although wet chemistry synthesis is extended to the preparation of other electrolytes by ammonium-assisted methods, it is only successful for ternary electrolytes. Developing a quaternary electrolyte through substitution is an effective way to improve the comprehensive properties of halide SSEs. Cationic substitution by the wet chemistry synthesis should be attempted.

(4) The compatibility of halide SSEs with high voltage cathodes has reached a satisfactory level, but the interface instability with Li metal anodes is still a difficult problem. Introducing an additional separator mitigates this dilemma, but the manufacturing process increases. The report of $Li_{0.388}Ta_{0.238}La_{0.475}Cl_3$ inspires researchers to improve the interfacial stability between halide SSEs and Li metal by designing electrolytes to *in situ* generate a gradient interfacial passivation layer.

Author contributions

All authors contributed to the writing and revision of the manuscript.

Conflicts of interest

There are no conflicts to declare.

Acknowledgements

References

1 Y. Bi, J. Tao, Y. Wu, L. Li, Y. Xu, E. Hu, B. Wu, J. Hu, C. Wang, J.-G. Zhang, Y. Qi and J. Xiao, *Science*, 2020, **370**, 1313–1317.

2 X. Fan and C. Wang, *Chem. Soc. Rev.*, 2021, **50**, 10486–10566.

3 T. Liu, J. Liu, L. Li, L. Yu, J. Diao, T. Zhou, S. Li, A. Dai, W. Zhao, S. Xu, Y. Ren, L. Wang, T. Wu, R. Qi, Y. Xiao, J. Zheng, W. Cha, R. Harder, I. Robinson, J. Wen, J. Lu, F. Pan and K. Amine, *Nature*, 2022, **606**, 305–312.

4 L. Wang, T. Liu, T. Wu and J. Lu, *Nature*, 2022, **611**, 61–67.

5 F. Wu, J. Maier and Y. Yu, *Chem. Soc. Rev.*, 2020, **49**, 1569–1614.

6 Y. Gao, Z. Pan, J. Sun, Z. Liu and J. Wang, *Nano-Micro Lett.*, 2022, **14**, 94.

7 Y. Tian, G. Zeng, A. Rutt, T. Shi, H. Kim, J. Wang, J. Koettgen, Y. Sun, B. Ouyang, T. Chen, Z. Lun, Z. Rong, K. Persson and G. Ceder, *Chem. Rev.*, 2021, **121**, 1623–1669.

8 X. Fan, C. Zhong, J. Liu, J. Ding, Y. Deng, X. Han, L. Zhang, W. Hu, D. P. Wilkinson and J. Zhang, *Chem. Rev.*, 2022, **122**, 17155–17239.

9 B. S. Vishnugopi, E. Kazyak, J. A. Lewis, J. Nanda, M. T. McDowell, N. P. Dasgupta and P. P. Mukherjee, *ACS Energy Lett.*, 2021, **6**, 3734–3749.

10 C. Sun, J. Liu, Y. Gong, D. P. Wilkinson and J. Zhang, *Nano Energy*, 2017, **33**, 363–386.

11 Y. Zheng, Y. Yao, J. Ou, M. Li, D. Luo, H. Dou, Z. Li, K. Amine, A. Yu and Z. Chen, *Chem. Soc. Rev.*, 2020, **49**, 8790–8839.

12 B. Tao, C. Ren, H. Li, B. Liu, X. Jia, X. Dong, S. Zhang and H. Chang, *Adv. Funct. Mater.*, 2022, **32**, 2203551.

13 R. Chen, Q. Li, X. Yu, L. Chen and H. Li, *Chem. Rev.*, 2020, **120**, 6820–6877.

14 K. B. Hatzell, *Matter*, 2021, **3**, 2533–2535.

15 T. Yu, X. Yang, R. Yang, X. Bai, G. Xu, S. Zhao, Y. Duan, Y. Wu and J. Wang, *J. Alloys Compd.*, 2021, **885**, 161013.

16 D. Wu, L. Chen, H. Li and F. Wu, *Appl. Phys. Lett.*, 2022, **121**, 120502.

17 Y. C. Yin, J. T. Yang, J. D. Luo, G. X. Lu, Z. Huang, J. P. Wang, P. Li, F. Li, Y. C. Wu, T. Tian, Y. F. Meng, H. S. Mo, Y. H. Song, J. N. Yang, L. Z. Feng, T. Ma, W. Wen, K. Gong, L. J. Wang, H. X. Ju, Y. Xiao, Z. Li, X. Tao and H. B. Yao, *Nature*, 2023, **616**, 77–83.

18 J. Janek and W. G. Zeier, *Nat. Energy*, 2023, **8**, 230–240.

19 H. Kwak, S. Wang, J. Park, Y. Liu, K. T. Kim, Y. Choi, Y. Mo and Y. S. Jung, *ACS Energy Lett.*, 2022, **7**, 1776–1805.

20 Y. Nikodimos, W. N. Su and B. J. Hwang, *Adv. Energy Mater.*, 2023, **13**, 2202854.

21 H. Wu, H. Han, Z. Yan, Q. Zhao and J. Chen, *J. Solid State Electrochem.*, 2022, **26**, 1791–1808.

22 J. Liang, X. Li, K. R. Adair and X. Sun, *Acc. Chem. Res.*, 2021, **54**, 1023–1033.

23 C. Wang, J. Liang, J. T. Kim and X. Sun, *Sci. Adv.*, 2022, **8**, eadc9516.

24 J. Liang, X. Li, S. Wang, K. R. Adair, W. Li, Y. Zhao, C. Wang, Y. Hu, L. Zhang, S. Zhao, S. Lu, H. Huang, R. Li, Y. Mo and X. Sun, *J. Am. Chem. Soc.*, 2020, **142**, 7012–7022.

25 X. Li, J. Liang, J. Luo, M. Norouzi Banis, C. Wang, W. Li, S. Deng, C. Yu, F. Zhao, Y. Hu, T.-K. Sham, L. Zhang, S. Zhao, S. Lu, H. Huang, R. Li, K. R. Adair and X. Sun, *Energy Environ. Sci.*, 2019, **12**, 2665–2671.

26 W. Li, J. Liang, M. Li, K. R. Adair, X. Li, Y. Hu, Q. Xiao, R. Feng, R. Li, L. Zhang, S. Lu, H. Huang, S. Zhao, T.-K. Sham and X. Sun, *Chem. Mater.*, 2020, **32**, 7019–7027.

27 S. Wang, Q. Bai, A. M. Nolan, Y. Liu, S. Gong, Q. Sun and Y. Mo, *Angew. Chem., Int. Ed.*, 2019, **58**, 8039–8043.

28 Y. Han, S. H. Jung, H. Kwak, S. Jun, H. H. Kwak, J. H. Lee, S. T. Hong and Y. S. Jung, *Adv. Energy Mater.*, 2021, **11**, 2100126.

29 M. Jiang, S. Mukherjee, Z. W. Chen, L. X. Chen, M. L. Li, H. Y. Xiao, C. Gao and C. V. Singh, *Phys. Chem. Chem. Phys.*, 2020, **22**, 22758–22767.

30 D. C. Ginnings and T. E. Phipps, *J. Am. Chem. Soc.*, 1930, **52**, 1340–1345.

31 K. Ryoji, T. Yasuo, M. Masashi and Y. Osamu, *Chem. Lett.*, 1989, **18**, 223–226.

32 C. Li, L. Gu and J. Maier, *Adv. Funct. Mater.*, 2012, **22**, 1145–1149.

33 T. Asano, A. Sakai, S. Ouchi, M. Sakaida, A. Miyazaki and S. Hasegawa, *Adv. Mater.*, 2018, **30**, 1803075.

34 X. Li, J. Liang, X. Yang, K. R. Adair, C. Wang, F. Zhao and X. Sun, *Energy Environ. Sci.*, 2020, **13**, 1429–1461.

35 S. R. Combs, P. K. Todd, P. Gorai and A. E. Maughan, *J. Electrochem. Soc.*, 2022, **169**, 040551.

36 J. Liang, X. Li, J. T. Kim, X. Hao, H. Duan, R. Li and X. Sun, *Angew. Chem., Int. Ed.*, 2023, **62**, e202217081.

37 J. Y. Huang, K. Iputera, A. Jena, Z. Tong, D. H. Wei, S. F. Hu and R. S. Liu, *J. Chin. Chem. Soc.*, 2022, **69**, 1233–1241.

38 X. Li, J. Liang, K. R. Adair, J. Li, W. Li, F. Zhao, Y. Hu, T. K. Sham, L. Zhang, S. Zhao, S. Lu, H. Huang, R. Li, N. Chen and X. Sun, *Nano Lett.*, 2020, **20**, 4384–4392.

39 Q. Shao, C. Yan, M. Gao, W. Du, J. Chen, Y. Yang, J. Gan, Z. Wu, W. Sun, Y. Jiang, Y. Liu, M. Gao and H. Pan, *ACS Appl. Mater. Interfaces*, 2022, **14**, 8095–8105.

40 S. Muy, J. Voss, R. Schlem, R. Koerver, S. J. Sedlmaier, F. Maglia, P. Lamp, W. G. Zeier and Y. Shao-Horn, *iScience*, 2019, **16**, 270–282.

41 R. Schlem, S. Muy, N. Prinz, A. Banik, Y. Shao-Horn, M. Zobel and W. G. Zeier, *Adv. Energy Mater.*, 2020, **10**, 1903719.

42 P. Molaiyan, S. E. Mailhiot, K. Voges, A. M. Kantola, T. Hu, P. Michalowski, A. Kwade, V.-V. Telkki and U. Lassi, *Mater. Des.*, 2023, **227**, 111690.

43 J. Park, D. Han, H. Kwak, Y. Han, Y. J. Choi, K.-W. Nam and Y. S. Jung, *Chem. Eng. J.*, 2021, **425**, 130630.

44 K.-H. Park, K. Kaup, A. Assoud, Q. Zhang, X. Wu and L. F. Nazar, *ACS Energy Lett.*, 2020, **5**, 533–539.

45 L. Zhou, C. Y. Kwok, A. Shyamsunder, Q. Zhang, X. Wu and L. F. Nazar, *Energy Environ. Sci.*, 2020, **13**, 2056–2063.

46 L. Zhou, T.-T. Zuo, C. Y. Kwok, S. Y. Kim, A. Assoud, Q. Zhang, J. Janek and L. F. Nazar, *Nat. Energy*, 2022, **7**, 83–93.

47 N. Tanibata, M. Kato, S. Takimoto, H. Takeda, M. Nakayama and H. Sumi, *Adv. Energy Sustainability Res.*, 2020, **1**, 2000025.

48 H. Kwak, J. Lyoo, J. Park, Y. Han, R. Asakura, A. Remhof, C. Battaglia, H. Kim, S.-T. Hong and Y. S. Jung, *Energy Storage Mater.*, 2021, **37**, 47–54.

49 J. Park, J. P. Son, W. Ko, J.-S. Kim, Y. Choi, H. Kim, H. Kwak, D.-H. Seo, J. Kim and Y. S. Jung, *ACS Energy Lett.*, 2022, **7**, 3293–3301.

50 D. Park, K. Kim, G. H. Chun, B. C. Wood, J. H. Shim and S. Yu, *J. Mater. Chem. A*, 2021, **9**, 23037–23045.

51 Y. Qie, S. Wang, S. Fu, H. Xie, Q. Sun and P. Jena, *J. Phys. Chem. Lett.*, 2020, **11**, 3376–3383.

52 Y. Lian, M. Wu, B. Xu, B. He, G. Liu, J. Shi, Q. Kuang, H. Wang and C. Ouyang, *J. Mater. Chem. A*, 2023, **11**, 1906–1919.

53 R. Li, K. Xu, K. Liu, R. Si and Z. Zhang, *Chem. Mater.*, 2022, **34**, 8356–8365.

54 H. Huang, C. Chi, J. Zhang, X. Zheng, Y. Wu, J. Shen, X. Wang and S. Wang, *ACS Appl. Mater. Interfaces*, 2022, **14**, 36864–36874.

55 H. Huang, H.-H. Wu, C. Chi, Y. Yang, J. Zheng, B. Huang and S. Wang, *J. Mater. Chem. A*, 2021, **9**, 26256–26265.

56 E. A. Wu, S. Banerjee, H. Tang, P. M. Richardson, J.-M. Doux, J. Qi, Z. Zhu, A. Grenier, Y. Li, E. Zhao, G. Deysher, E. Sebti, H. Nguyen, R. Stephens, G. Verbist, K. W. Chapman, R. J. Clément, A. Banerjee, Y. S. Meng and S. P. Ong, *Nat. Commun.*, 2021, **12**, 1256.

57 E. Sebti, J. Qi, P. M. Richardson, P. Ridley, E. A. Wu, S. Banerjee, R. Giovine, A. Cronk, S.-Y. Ham, Y. S. Meng, S. P. Ong and R. J. Clément, *J. Mater. Chem. A*, 2022, **10**, 21565–21578.

58 R. Schlem, A. Banik, M. Eckardt, M. Zobel and W. G. Zeier, *ACS Appl. Energy Mater.*, 2020, **3**, 10164–10173.

59 F. Hussain, P. Yu, J. Zhu, H. Xia, Y. Zhao and W. Xia, *Adv. Theory Simul.*, 2023, **6**, 2200569.

60 N. Flores-Gonzalez, N. Minafra, G. Dewald, H. Reardon, R. I. Smith, S. Adams, W. G. Zeier and D. H. Gregory, *ACS Mater. Lett.*, 2021, **3**, 652–657.

61 X. Li, J. Liang, N. Chen, J. Luo, K. R. Adair, C. Wang, M. N. Banis, T. K. Sham, L. Zhang, S. Zhao, S. Lu, H. Huang, R. Li and X. Sun, *Angew. Chem., Int. Ed.*, 2019, **58**, 16427–16432.

62 X. Luo, D. Cai, X. Wang, X. Xia, C. Gu and J. Tu, *ACS Appl. Mater. Interfaces*, 2022, **14**, 29844–29855.

63 C. Wang, J. Liang, J. Luo, J. Liu, X. Li, F. Zhao, R. Li, H. Huang, S. Zhao, L. Zhang, J. Wang and X. Sun, *Sci. Adv.*, 2021, **7**, eabh1896.

64 D. Zagorac, H. Muller, S. Ruehl, J. Zagorac and S. Rehme, *J. Appl. Crystallogr.*, 2019, **52**, 918–925.

65 Z. Wang, X. Lin, Y. Han, J. Cai, S. Wu, X. Yu and J. Li, *Nano Energy*, 2021, **89**, 106337.

66 W. Qiu, Y. Wang and J. Liu, *Wiley Interdiscip. Rev.: Comput. Mol. Sci.*, 2022, **12**, e1592.

67 A. Vasylenko, J. Gamon, B. B. Duff, V. V. Gusev, L. M. Daniels, M. Zanella, J. F. Shin, P. M. Sharp, A. Morscher, R. Chen, A. R. Neale, L. J. Hardwick, J. B. Claridge, F. Blanc, M. W. Gaultois, M. S. Dyer and M. J. Rosseinsky, *Nat. Commun.*, 2021, **12**, 5561.

68 F. Li, X. Cheng, L. L. Lu, Y. C. Yin, J. D. Luo, G. Lu, Y. F. Meng, H. Mo, T. Tian, J. T. Yang, W. Wen, Z. P. Liu, G. Zhang, C. Shang and H. B. Yao, *Nano Lett.*, 2022, **22**, 2461–2469.

69 L. Kahle, A. Marcolongo and N. Marzari, *Energy Environ. Sci.*, 2020, **13**, 928–948.

70 J. Qi, S. Banerjee, Y. Zuo, C. Chen, Z. Zhu, M. L. Holekevi Chandrappa, X. Li and S. P. Ong, *Mater. Today Phys.*, 2021, **21**, 100463.

71 T. H. Wan and F. Ciucci, *ACS Appl. Energy Mater.*, 2021, **4**, 7930–7941.

72 W. Chen, Y. Li, D. Feng, C. Lv, H. Li, S. Zhou, Q. Jiang, J. Yang, Z. Gao, Y. He and J. Luo, *J. Power Sources*, 2023, **561**, 232720.

73 Z. Xu, X. Chen, R. Chen, X. Li and H. Zhu, *npj Comput. Mater.*, 2020, **6**, 47.

74 Y. Yu, Z. Wang and G. Shao, *J. Mater. Chem. A*, 2021, **9**, 25585–25594.

75 S. Zhang, J. Ma, S. Dong and G. Cui, *Electrochem. Energy Rev.*, 2023, **6**, 4.

76 R. D. Shannon, *Acta Crystallogr., Sect. A: Found. Adv.*, 1976, **32**, 751–767.

77 A. D. Sendek, G. Cheon, M. Pasta and E. J. Reed, *J. Phys. Chem. C*, 2020, **124**, 8067–8079.

78 K. Kim, D. Park, H.-G. Jung, K. Y. Chung, J. H. Shim, B. C. Wood and S. Yu, *Chem. Mater.*, 2021, **33**, 3669–3677.

79 H. Chun, K. Nam, S. J. Hong, J. Kang and B. Han, *J. Mater. Chem. A*, 2021, **9**, 15605–15612.

80 Y. Liu, S. Wang, A. M. Nolan, C. Ling and Y. Mo, *Adv. Energy Mater.*, 2020, **10**, 2002356.

81 Z. Xu and H. Zhu, *Chem. Mater.*, 2020, **32**, 4618–4626.

82 Z. Xu, X. Chen, K. Liu, R. Chen, X. Zeng and H. Zhu, *Chem. Mater.*, 2019, **31**, 7425–7433.

83 R. Schlem, T. Bernges, C. Li, M. A. Kraft, N. Minafra and W. G. Zeier, *ACS Appl. Energy Mater.*, 2020, **3**, 3684–3691.

84 Y. Wang, W. D. Richards, S. P. Ong, L. J. Miara, J. C. Kim, Y. Mo and G. Ceder, *Nat. Mater.*, 2015, **14**, 1026–1031.

85 H. Kwak, D. Han, J. Lyoo, J. Park, S. H. Jung, Y. Han, G. Kwon, H. Kim, S. T. Hong, K. W. Nam and Y. S. Jung, *Adv. Energy Mater.*, 2021, **11**, 2003190.

86 K. Wang, Q. Ren, Z. Gu, C. Duan, J. Wang, F. Zhu, Y. Fu, J. Hao, J. Zhu, L. He, C. W. Wang, Y. Lu, J. Ma and C. Ma, *Nat. Commun.*, 2021, **12**, 4410.

87 H. Ito, K. Shitara, Y. Wang, K. Fujii, M. Yashima, Y. Goto, C. Moriyoshi, N. C. Rosero-Navarro, A. Miura and K. Tadanaga, *Adv. Sci.*, 2021, **8**, 2101413.

88 H. Wang, Y. Li, Y. Tang, D. Ye, T. He, H. Zhao and J. Zhang, *ACS Appl. Mater. Interfaces*, 2023, **15**, 5504–5511.

89 X. Li, J. Liang, J. T. Kim, J. Fu, H. Duan, N. Chen, R. Li, S. Zhao, J. Wang, H. Huang and X. Sun, *Adv. Mater.*, 2022, **34**, 2200856.

90 R. Schlem, A. Banik, S. Ohno, E. Suard and W. G. Zeier, *Chem. Mater.*, 2021, **33**, 327–337.

91 M. Gombotz and H. M. R. Wilkening, *ACS Sustainable Chem. Eng.*, 2021, **9**, 743–755.

92 K. Wang, Z. Gu, Z. Xi, L. Hu and C. Ma, *Nat. Commun.*, 2023, **14**, 1396.

93 N. Flores-González, M. López, N. Minafra, J. Bohnenberger, F. Viñes, S. Rudić, I. Krossing, W. G. Zeier, F. Illas and D. H. Gregory, *J. Mater. Chem. A*, 2022, **10**, 13467–13475.

94 F. Hussain, J. Zhu, H. Xia, Y. Zhao and W. Xia, *J. Phys. Chem. C*, 2022, **126**, 13105–13113.

95 S. Hyun, H. Chun, M. Hong, J. Kang and B. Han, *J. Mater. Chem. A*, 2023, **11**, 4272–4279.

96 J. Liang, E. Maas, J. Luo, X. Li, N. Chen, K. R. Adair, W. Li, J. Li, Y. Hu, J. Liu, L. Zhang, S. Zhao, S. Lu, J. Wang, H. Huang, W. Zhao, S. Parnell, R. I. Smith, S. Ganapathy, M. Wagemaker and X. Sun, *Adv. Energy Mater.*, 2022, **12**, 2103921.

97 S. Y. Kim, K. Kaup, K.-H. Park, A. Assoud, L. Zhou, J. Liu, X. Wu and L. F. Nazar, *ACS Mater. Lett.*, 2021, **3**, 930–938.

98 Y. Huang, Y. Yu, H. Xu, X. Zhang, Z. Wang and G. Shao, *J. Mater. Chem. A*, 2021, **9**, 14969–14976.

99 D. Park, H. Park, Y. Lee, S. O. Kim, H. G. Jung, K. Y. Chung, J. H. Shim and S. Yu, *ACS Appl. Mater. Interfaces*, 2020, **12**, 34806–34814.

100 G. Xu, L. Luo, J. Liang, S. Zhao, R. Yang, C. Wang, T. Yu, L. Wang, W. Xiao, J. Wang, J. Yu and X. Sun, *Nano Energy*, 2022, **92**, 106674.

101 B. He, A. Ye, S. Chi, P. Mi, Y. Ran, L. Zhang, X. Zou, B. Pu, Q. Zhao, Z. Zou, D. Wang, W. Zhang, J. Zhao, M. Avdeev and S. Shi, *Sci. Data*, 2020, **7**, 153.

102 B. He, P. Mi, A. Ye, S. Chi, Y. Jiao, L. Zhang, B. Pu, Z. Zou, W. Zhang, M. Avdeev, S. Adams, J. Zhao and S. Shi, *Acta Mater.*, 2021, **203**, 116490.

103 E. van der Maas, W. Zhao, Z. Cheng, T. Famprikis, M. Thijs, S. R. Parnell, S. Ganapathy and M. Wagemaker, *J. Phys. Chem. C*, 2023, **127**, 125–132.

104 Z. Liu, S. Ma, J. Liu, S. Xiong, Y. Ma and H. Chen, *ACS Energy Lett.*, 2021, **6**, 298–304.

105 H. Kwak, D. Han, J. P. Son, J. S. Kim, J. Park, K.-W. Nam, H. Kim and Y. S. Jung, *Chem. Eng. J.*, 2022, **437**, 135413.

106 E. van der Maas, T. Famprikis, S. Pieters, J. P. Dijkstra, Z. Li, S. R. Parnell, R. I. Smith, E. R. H. van Eck, S. Ganapathy and M. Wagemaker, *J. Mater. Chem. A*, 2023, **11**, 4559–4571.

107 B. Helm, R. Schlem, B. Wankmiller, A. Banik, A. Gautam, J. Ruhl, C. Li, M. R. Hansen and W. G. Zeier, *Chem. Mater.*, 2021, **33**, 4773–4782.

108 J. Fu, S. Yang, J. Hou, L. Azhari, Z. Yao, X. Ma, Y. Liu, P. Vanaphuti, Z. Meng, Z. Yang, Y. Zhong and Y. Wang, *J. Power Sources*, 2023, **556**, 232465.

109 X. Luo, X. Wu, J. Xiang, D. Cai, M. Li, X. Wang, X. Xia, C. Gu and J. Tu, *ACS Appl. Mater. Interfaces*, 2021, **13**, 47610–47618.

110 S. Zhang, F. Zhao, S. Wang, J. Liang, J. Wang, C. Wang, H. Zhang, K. Adair, W. Li, M. Li, H. Duan, Y. Zhao, R. Yu, R. Li, H. Huang, L. Zhang, S. Zhao, S. Lu, T. K. Sham, Y. Mo and X. Sun, *Adv. Energy Mater.*, 2021, **11**, 2100836.

111 X. Chen, Z. Jia, H. Lv, C. Wang, N. Zhao and X. Guo, *J. Power Sources*, 2022, **545**, 231939.

112 S. Chen, C. Yu, S. Chen, L. Peng, C. Liao, C. Wei, Z. Wu, S. Cheng and J. Xie, *Chin. Chem. Lett.*, 2022, **33**, 4635–4639.

113 H. Zhang, Z. Yu, H. Chen, Y. Zhou, X. Huang and B. Tian, *J. Energy Chem.*, 2023, **79**, 348–356.

114 H. Kwak, J. S. Kim, D. Han, J. S. Kim, J. Park, G. Kwon, S. M. Bak, U. Heo, C. Park, H. W. Lee, K. W. Nam, D. H. Seo and Y. S. Jung, *Nat. Commun.*, 2023, **14**, 2459.

115 W. Li, Z. Chen, Y. Chen, W. Duan, G. Liu, Y. Lv, H. Yang and L. Yao, *Chem. Eng. J.*, 2023, **455**, 140509.

116 H. Zhang, Z. Zeng, X. Shi, C. H. Wang and Y. Du, *EcoMat*, 2023, **5**, e12315.

117 Y. Ishiguro, K. Ueno, S. Nishimura, G. Iida and Y. Igarashib, *Chem. Lett.*, 2023, **52**, 237–241.

118 T. Yu, J. Liang, L. Luo, L. Wang, F. Zhao, G. Xu, X. Bai, R. Yang, S. Zhao, J. Wang, J. Yu and X. Sun, *Adv. Energy Mater.*, 2021, **11**, 2101915.

119 X. Shi, Z. Zeng, M. Sun, B. Huang, H. Zhang, W. Luo, Y. Huang, Y. Du and C. Yan, *Nano Lett.*, 2021, **21**, 9325–9331.

120 X. Shi, Z. Zeng, H. Zhang, B. Huang, M. Sun, H. H. Wong, Q. Lu, W. Luo, Y. Huang, Y. Du and C. H. Yan, *Small Methods*, 2021, **5**, 2101002.

121 M. A. Plass, S. Bette, R. E. Dinnebier and B. V. Lotsch, *Chem. Mater.*, 2022, **34**, 3227–3235.

122 T. Jeon and S. C. Jung, *J. Mater. Chem. A*, 2023, **11**, 4334–4344.

123 C. Yu, Y. Li, K. R. Adair, W. Li, K. Goubitz, Y. Zhao, M. J. Willans, M. A. Thijs, C. Wang, F. Zhao, Q. Sun, S. Deng, J. Liang, X. Li, R. Li, T.-K. Sham, H. Huang, S. Lu, S. Zhao, L. Zhang, L. van Eijck, Y. Huang and X. Sun, *Nano Energy*, 2020, **77**, 105097.

124 E. Sebti, H. A. Evans, H. Chen, P. M. Richardson, K. M. White, R. Giovine, K. P. Koirala, Y. Xu, E. Gonzalez-Correa, C. Wang, C. M. Brown, A. K. Cheetham, P. Canepa and R. J. Clement, *J. Am. Chem. Soc.*, 2022, **144**, 5795–5811.

125 Y. Wang, Y. Wu, Z. Wang, L. Chen, H. Li and F. Wu, *J. Mater. Chem. A*, 2022, **10**, 4517–4532.

126 Y. Ni, C. Huang, H. Liu, Y. Liang and L. Z. Fan, *Adv. Funct. Mater.*, 2022, **32**, 2205998.

127 E. Umeshbabu, S. Maddukuri, Y. Hu, M. Fichtner and A. R. Munnangi, *ACS Appl. Mater. Interfaces*, 2022, **14**, 25448–25456.

128 Y. Kim and S. Choi, *J. Power Sources*, 2023, **567**, 232962.

129 S. Chen, C. Yu, C. Wei, L. Peng, S. Cheng and J. Xie, *Chin. Chem. Lett.*, 2023, **34**, 107544.

130 Ö. U. Kudu, T. Famprikis, B. Fleutot, M.-D. Braida, T. Le Mercier, M. S. Islam and C. Masquelier, *J. Power Sources*, 2018, **407**, 31–43.

131 H.-W. Liu, C.-C. Lin, P.-Y. Chang, S.-C. Haw, H.-S. Sheu, J.-M. Chen, C.-C. Chen, R.-J. Jeng and N.-L. Wu, *J. Solid State Electrochem.*, 2022, **26**, 2089–2096.

132 T. Ma, Z. Wang, D. Wu, P. Lu, X. Zhu, M. Yang, J. Peng, L. Chen, H. Li and F. Wu, *Energy Environ. Sci.*, 2023, **16**, 2142–2152.

133 M. Yang, L. Chen, H. Li and F. Wu, *Energy Mater. Adv.*, 2022, **2022**, 9842651.

134 L. Zhu, Y. Wang, J. Chen, W. Li, T. Wang, J. Wu, S. Han, Y. Xia, Y. Wu, M. Wu, F. Wang, Y. Zheng, L. Peng, J. Liu, L. Chen and W. Tang, *Sci. Adv.*, 2022, **8**, eabj7698.

135 P. Lu, D. Wu, L. Chen, H. Li and F. Wu, *Electrochem. Energy Rev.*, 2022, **5**, 3.

136 A. Sharafi, E. Kazyak, A. L. Davis, S. Yu, T. Thompson, D. J. Siegel, N. P. Dasgupta and J. Sakamoto, *Chem. Mater.*, 2017, **29**, 7961–7968.

137 Y. Zhu and Y. Mo, *Angew. Chem., Int. Ed.*, 2020, **59**, 17472–17476.

138 S. Wang, X. Xu, C. Cui, C. Zeng, J. Liang, J. Fu, R. Zhang, T. Zhai and H. Li, *Adv. Funct. Mater.*, 2022, **32**, 2108805.

139 J.-S. Kim, S. Soo Shin, J.-H. Lee, B.-K. Kim and H. Kim, *Appl. Surf. Sci.*, 2022, **574**, 151621.

140 R. L. Sacci, T. H. Bennett, A. R. Drews, V. Anandan, M. J. Kirkham, L. L. Daemen and J. Nanda, *J. Mater. Chem. A*, 2021, **9**, 990–996.

141 E. McCalla, M. T. Sougrati, G. Rousse, E. J. Berg, A. Abakumov, N. Recham, K. Ramesha, M. Sathiya, R. Dominko, G. Van Tendeloo, P. Novak and J. M. Tarascon, *J. Am. Chem. Soc.*, 2015, **137**, 4804–4814.

142 B. Zahiri, A. Patra, C. Kiggins, A. X. B. Yong, E. Ertekin, J. B. Cook and P. V. Braun, *Nat. Mater.*, 2021, **20**, 1392–1400.

143 X. Miao, S. Guan, C. Ma, L. Li and C. W. Nan, *Adv. Mater.*, 2023, DOI: 10.1002/adma.202206402.

144 I. Kochetkov, T.-T. Zuo, R. Ruess, B. Singh, L. Zhou, K. Kaup, J. Janek and L. Nazar, *Energy Environ. Sci.*, 2022, **15**, 3933–3944.

145 G. H. Chun, J. H. Shim and S. Yu, *ACS Appl. Mater. Interfaces*, 2022, **14**, 1241–1248.

146 P. Bonnick and J. Muldoon, *Energy Environ. Sci.*, 2022, **15**, 1840–1860.

147 G. Wang, M. Zhu, Y. Zhang, C. Song, X. Zhu, Z. Huang, Y. Zhang, F. Yu, G. Xu, M. Wu, H. K. Liu, S. X. Dou and C. Wu, *InfoMat*, 2022, **4**, e12293.

148 K. B. Hatzell, X. C. Chen, C. L. Cobb, N. P. Dasgupta, M. B. Dixit, L. E. Marbella, M. T. McDowell, P. P. Mukherjee, A. Verma, V. Viswanathan, A. S. Westover and W. G. Zeier, *ACS Energy Lett.*, 2020, **5**, 922–934.

149 D. K. Singh, T. Fuchs, C. Krempaszky, B. Mogwitz, S. Burkhardt, F. H. Richter and J. Janek, *Adv. Funct. Mater.*, 2022, **33**, 2211067.

150 L. M. Riegger, R. Schlem, J. Sann, W. G. Zeier and J. Janek, *Angew. Chem., Int. Ed.*, 2021, **60**, 6718–6723.

151 Y. Zhu, X. He and Y. Mo, *J. Mater. Chem. A*, 2016, **4**, 3253–3266.

152 Y. Fu and C. Ma, *Sci. China Mater.*, 2021, **64**, 1378–1385.

153 W. Ji, D. Zheng, X. Zhang, T. Ding and D. Qu, *J. Mater. Chem. A*, 2021, **9**, 15012–15018.

154 H. Zhang, Z. Yu, J. Cheng, H. Chen, X. Huang and B. Tian, *Chin. Chem. Lett.*, 2023, DOI: 10.1016/j.cclet.2023.108228.

155 T. Koç, M. Hallot, E. Quemin, B. Hennequart, R. Dugas, A. M. Abakumov, C. Lethien and J.-M. Tarascon, *ACS Energy Lett.*, 2022, **7**, 2979–2987.

156 T. Koç, F. Marchini, G. Rousse, R. Dugas and J.-M. Tarascon, *ACS Appl. Energy Mater.*, 2021, **4**, 13575–13585.

157 C. Rosenbach, F. Walther, J. Ruhl, M. Hartmann, T. A. Hendriks, S. Ohno, J. Janek and W. G. Zeier, *Adv. Energy Mater.*, 2023, **13**, 2203673.

158 J. Jang, Y.-T. Chen, G. Deysher, D. Cheng, S.-Y. Ham, A. Cronk, P. Ridley, H. Yang, B. Sayahpour, B. Han, W. Li, W. Yao, E. A. Wu, J.-M. Doux, L. H. B. Nguyen, J. A. S. Oh, D. H. S. Tan and Y. S. Meng, *ACS Energy Lett.*, 2022, **7**, 2531–2539.

159 Y. Subramanian, R. Rajagopal and K.-S. Ryu, *J. Alloys Compd.*, 2023, **940**, 168867.

160 X. Xu, G. Du, C. Cui, J. Liang, C. Zeng, S. Wang, Y. Ma and H. Li, *ACS Appl. Mater. Interfaces*, 2022, **14**, 39951–39958.

161 R. Yu, C. Wang, H. Duan, M. Jiang, A. Zhang, A. Fraser, J. Zuo, Y. Wu, Y. Sun, Y. Zhao, J. Liang, J. Fu, S. Deng, Z. Ren, G. Li, H. Huang, R. Li, N. Chen, J. Wang, X. Li, C. V. Singh and X. Sun, *Adv. Mater.*, 2023, **35**, 2207234.

162 T. A. Hendriks, M. A. Lange, E. M. Kiens, C. Baeumer and W. G. Zeier, *Batteries Supercaps*, 2023, **6**, e202200544.

163 C. Wang, J. Liang, M. Jiang, X. Li, S. Mukherjee, K. Adair, M. Zheng, Y. Zhao, F. Zhao, S. Zhang, R. Li, H. Huang, S. Zhao, L. Zhang, S. Lu, C. V. Singh and X. Sun, *Nano Energy*, 2020, **76**, 105015.

164 Q. Luo, C. Yu, C. Wei, S. Chen, S. Chen, Z. Jiang, L. Peng, S. Cheng and J. Xie, *Ceram. Int.*, 2023, **49**, 11485–11493.

165 C. Zhao, J. Liang, X. Li, N. Holmes, C. Wang, J. Wang, F. Zhao, S. Li, Q. Sun, X. Yang, J. Liang, X. Lin, W. Li, R. Li, S. Zhao, H. Huang, L. Zhang, S. Lu and X. Sun, *Nano Energy*, 2020, **75**, 105036.

166 J. S. Kim, S. Jung, H. Kwak, Y. Han, S. Kim, J. Lim, Y. M. Lee and Y. S. Jung, *Energy Storage Mater.*, 2023, **55**, 193–204.